Article

Imbalance of circuit plasticity and consolidation in autism model marmosets is adjusted by oxytocin administration

Jun Noguchi[1*], Satoshi Watanabe[1], Tomofumi Oga[1], Risa Isoda[1], Keiko Nakagaki[1], Kazuhisa Sakai[1], Kayo Sumida[2], Kohei Hoshino[2], Koichi Saito[2], Izuru Miyawaki[3], Eriko Sugano[4], Hiroshi Tomita[4], Hiroaki Mizukami[5], Akiya Watakabe[6], Tetsuo Yamamori[6] & Noritaka Ichinohe[1*]

[1] Department of Ultrastructural Research, National Institute of Neuroscience, National Center of Neurology and Psychiatry, Tokyo, Japan. [2] Environmental Health Science Laboratory, Sumitomo Chemical Co., Ltd., Konohana-ku, Osaka, Japan. [3] Preclinical Research Laboratories, Sumitomo Pharma Co., Ltd., Konohana-ku, Osaka, Japan.[4] Laboratory of Visual Neuroscience, Graduate Course in Biological Sciences, Iwate University, Iwate, Japan. [5] Division of Genetic Therapeutics, Jichi Medical University, Tochigi, Japan. [6] Laboratory for Molecular Analysis of Higher Brain Function, Center for Brain Science, RIKEN, Saitama, Japan.

*Correspondence should be addressed to J.N. (jnoguchi@ncnp.go.jp) or N.I. (nichino@ncnp.go.jp).

Abstract

Impairments in the experience-dependent elaboration of neural circuits are assumed to underlie autism spectrum disorder (ASD). However, the phenotype underlying synaptic plasticity is poorly understood. Here, we used a valproic acid–induced ASD marmoset model and in vivo two-photon microscopy to investigate the structural dynamics of dendritic spines in the dorsomedial prefrontal cortex, which is involved in ASD core symptoms. In model marmosets compared to controls, spine turnover was upregulated and spines were actively generated in clusters. Clustered emerging spines were predominant in carryover of generated spines in the model marmosets. Presynaptic boutons of local axons, but not long-range commissural axons, showed hyperdynamic turnover. Furthermore, nasal oxytocin administration reduced the clustered emergence of spines. Finally, we confirmed the high molecular conformity of adult animal models with human ASD. Our study suggests that an altered balance between synaptic plasticity and consolidation underlies ASD, and may be a potential therapeutic target.

Introduction

Autism spectrum disorder (ASD) is a developmental disorder characterized by deficits in social communication and interaction, stereotyped behaviors, and sensory hypo- and hypersensitivity[1, 2]. Individuals with ASD often have learning disabilities and have difficulty learning to recognize verbal or non-verbal social information[3]. Learning impairments in ASD may be associated with the formation of inflexible habits, ritualistic behavior[4], and difficulty in adapting quickly to a temporally changing environment, which may limit sociality[5]. Proper refinement of neural networks during learning is achieved by coordinated synaptic remodeling, including the generation and elimination of dendritic spines[6-8]. In ASD, these synaptic functions are likely maladjusted. ASD-related genes include a substantial number of synapse-related genes and those that regulate these genes' expression. Humans with ASD and ASD model animals exhibit altered dendritic spine morphology[9-11]. In addition to the aberrant synaptic E/I balance[12], accelerations in

spine turnover in motor cortices and the primary sensory area are the dominant phenotype in ASD model mice[13, 14], including inbred BTBR[15], Fmr1 knock-out[16, 17], and Neurolign-3 R451C knock-in mice[15], as well as those with 15q11–13 duplications[15]. To understand the pathophysiology of ASD, it is essential to elucidate the mechanisms of altered features on circuit remodeling in ASD-related brain structures, especially in the context of synaptic disorders.

Therapeutic approaches for the core symptoms of ASD have not yet been established. Oxytocin is a potentially effective treatment for these symptoms, and investigation of its mechanism of action is expected to provide necessary insights into its clinical use. Oxytocin is a neurohormone that is produced in the hypothalamus and released into the blood by the pituitary gland. The axons of oxytocin-producing neurons also project to several brain regions, where they release oxytocin as a neuropeptide[18]. Because oxytocin modifies the social skills of typically developed human individuals, and improves sociality in mouse ASD models[19-21], its potential as a therapeutic agent for ASD has long been anticipated. However, the therapeutic benefits of oxytocin in human clinical trials are currently inconclusive[22-25]. The reported variations in oxytocin efficacy are thought to be due to a combination of differences in doses, schedules, ASD subpopulations, and concomitant psychosocial interventions. In order to improve oxytocin treatments for ASD, it is critical to evaluate the mechanisms of the neurobiological effects of oxytocin administration in ASD.

The common marmoset (*Callithrix jacchus*), a small New World monkey, has attracted significant attention in ASD research due to its rich repertoire of social behaviors, a well-developed prefrontal cortex (PFC) that supports high-level social ability, and gene expression networks that are similar to those in humans[26]. Comparative studies on synapse biology showed that marmosets are more similar to humans than rodents in terms of their synaptic proteome[27]. We previously developed a marmoset model of ASD by orally administrating valproic acid (VPA)

to a pregnant marmoset and obtaining affected offspring[11]. The ASD model marmosets demonstrated deficits in higher social decision-making, a process that may require a well-developed PFC[28, 29]. In a reversal learning task that mimicked habit formation, the marmosets exhibited perseverance[30]. They also showed variations in brain structure and cell biology[11]. In particular, juvenile VPA-exposed model marmosets reproduced gene expression variations of human idiopathic ASD involving gene groups (modules) associated with the four major cell types of the brain: neurons, oligodendrocytes, astrocytes, and microglia, all of which are involved in synaptic plasticity[11, 31]. By contrast, rodent ASD models demonstrated human ASD–like changes in only some of the modules, and in fewer cell types[11]. Discrepancies in the therapeutic efficacy of candidate molecules between rodents and primates, including humans, may depend on differences in receptor molecules and their expression. For instance, differences between rodent and primate oxytocin systems suggest that primate models are superior for oxytocin research, which may lead to clinical applications[32]. These results support the high translational value of VPA-exposed marmosets as an ASD model.

The current study monitored the temporal remodeling of neural circuits using in vivo two-photon longitudinal imaging in an ASD model involving VPA-exposed adult marmosets. It investigated synaptic dynamics at 3-day intervals in the apical dendrites of pyramidal neurons in the primate-specific dorsomedial PFC (dmPFC). The dmPFC is involved in social cognition and habit formation, and is impaired in ASD[33]. Our study revealed that in VPA-exposed marmosets, turnover of postsynaptic dendritic spines was upregulated, and spines were actively generated in clusters but seemed to be rather randomly eliminated. Increased rates of clustered spine generation during learning have been reported to correlate with learning performance[34, 35]. Clustering of dynamic spines is also currently of interest in terms of disease pathogenesis and therapeutic efficacy[36]. A larger fraction of emergent spines survived in model animals than in controls, especially spines that appeared in clusters. These synaptic characteristics are consistent with the

behavioral characteristics of model animals in a reversal learning paradigm[30]. Furthermore, nasal administration of oxytocin reduced the clustered emergence of spines without affecting turnover rate. These results suggest that there is an imbalance in circuit plasticity and consolidation in ASD and that the regulation of these processes may be a therapeutic target of ASD.

Results

Two-photon imaging of the dendrites of PFC L2/3 pyramidal neurons in living marmosets

Dendritic spines are the postsynaptic sites of the most excitatory synapses in cortical pyramidal neurons. Changes in dendritic spine density have been observed in the brains of ASD individuals[9], and alterations in synaptic plasticity have been reported in ASD animal models[11, 37]. Moreover, increased generation and elimination rates of cortical dendritic spines have been reported in rodent ASD models[13-17]. In the present study, we used a marmoset ASD model to investigate spine dynamics in the dmPFC. We used three adult VPA-exposed marmosets and four adult unexposed (UE) marmosets (See **Methods**). We inoculated the marmoset dmPFC with adeno-associated virus (AAV) and expressed fluorescent proteins mainly in layer-2/3 pyramidal neurons[38]. To obtain sufficiently strong but sparse fluorescent protein expression on pyramidal neurons, we used the tetracyclin tTA–TRE expression system and the Thy1S promoter[38]. We constructed three AAV vectors: in one, the tTA component was under the control of the Thy1S promoter (AAV: Thy1S-tTA), while in the others, tdTomato (left hemisphere of all monkeys; red fluorescent protein) or mClover (right hemisphere of five monkeys; green fluorescent protein) was under the control of TRE (AAV:TRE-tdTomato; AAV:TRE-mClover)[38]. These AAV combinations showed better fluorescent protein brightness than cre-dependent AAV combinations (results not shown). The fluorescent protein–expressing neurons were locally distributed with an average diameter of 1.81 mm (range: 1.02–2.87) axially and 1.53 mm (range: 0.86–2.21) laterally. Post-experiment

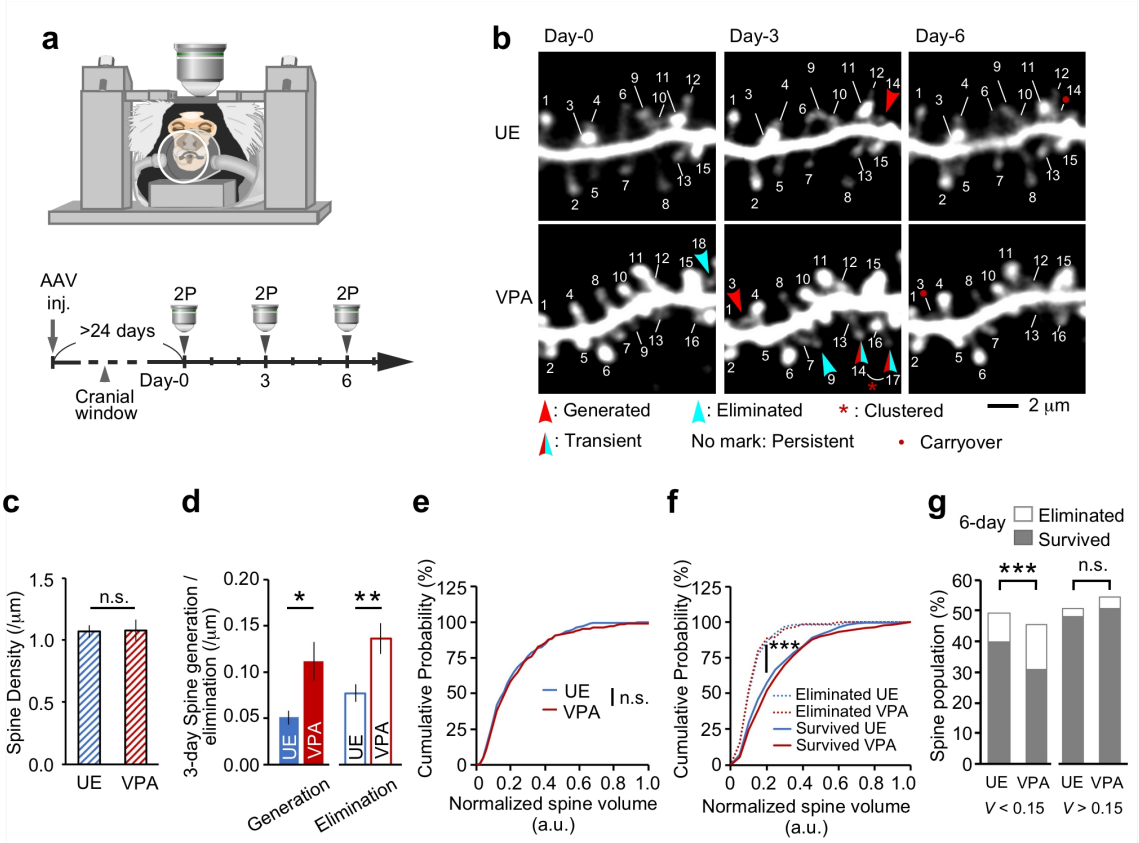

Fig. 1 In vivo two-photon imaging of mature marmoset dendrites. **a** A marmoset was anesthetized for two-photon (2P) imaging. The lower panel shows the experimental schema. **b** Longitudinal 2P imaging from the PFC layer 2/3 pyramidal neuron tuft dendrites. Every 3 days, the same dendrites were imaged in UE (unexposed; control animals) and VPA-exposed (ASD model) marmosets, and the same spines were labeled using the same numbers throughout the period. **c** Mean spine densities of dendrites (mean ± s.e.m.; P = 0.85, Mann-Whitney U test; *n* = 14 and 12 dendrites in four and three UE and VPA-exposed animals, respectively). **d** Three-day spine generation per unit dendrite length (mean ± s.e.m.; *P* = 0.0404, Mann-Whitney U test; the same dendrites as in (c)), and 3-day elimination (*P* = 0.0037). **e, f** Cumulative plots of the normalized spine volume distribution (e) (*P* = 0.72; Kolmogorov-Smirnov test; n = 536 and 473 spines in UE and VPA-exposed animals, respectively), and cumulative plots of eliminated UE, eliminated VPA-exposed, surviving UE, and surviving VPA-exposed spines during the 6-day observation (f) (*P* < 0.001; *n* = 65, 87, 471, and 386 spines, respectively). **g** The population of eliminated and surviving spines during the 6-day observation are shown separately for groups with a spine volume of *V* < 0.15 and *V* > 0.15 (*V* < 0.15; *P* = 0.001; Fisher's exact test; *n* = 50, 69, 214, and 146 spines as in (f)) (*V* > 0.15; *P* = 0.59; *n* = 15, 18, 257, and 240 spines as in (f)). ***P < 0.001; **P < 0.01; *P < 0.05; n.s., not significant.

immunohistochemistry using antibodies for Iba-1 and GFAP showed no obvious signs of activation of microglia or astrocytes, respectively (results not shown).

We performed time-lapse observation of the dmPFC using a two-photon microscope[38, 39] (Fig. 1a, b). We conducted three imaging sessions every 3 days. We found no significant differences

in dendritic spine density on apical tufts between the VPA-exposed and UE marmosets (Fig. 1c). Although there is a report of increased postmortem dendritic spine density in humans with ASD[9], spines on dendritic tufts have not been examined in human tissues. We next compared the spine generation and elimination rates between the VPA-exposed and UE groups (Fig. 1b, d). We found that the rates of both spine generation and elimination were approximately two-fold higher in VPA-exposed than UE marmosets (Fig. 1d). This is consistent with a previous report on the somatosensory barrel cortex in juvenile ASD mouse models (BTBR mouse, 15q11–13 duplication, Neuroligin mutant)[15], and the other on the visual cortex in an adult Fragile-X syndrome mouse model[17], both of which demonstrated increased rates of spine generation and elimination than wild-type animals.

Smaller spines in the ASD model marmoset were more prone to elimination

We then performed an analysis of spine volume, which is an important measure of synaptic weight. We calculated the normalized spine volume by dividing each spine's fluorescent intensity with the dendrite shaft intensity, and pooled the results of all dendrites (See **Methods** section for details). The results showed no significant difference in the distribution of spine volume between the VPA-exposed and UE groups (Fig. 1e). There was a significant difference in volume distribution between spines that were eliminated during the 6-day period and those that survived in both groups (Fig. 1f). The volume distribution of the VPA-exposed and UE groups did not differ when the eliminated and surviving groups were analyzed separately (Fig. 1f); however, for the smaller spines, the proportion of eliminated spines was significantly larger in the VPA-exposed group (Fig. 1g). As in previous studies[40, 41], spine elimination was more likely in smaller spines in UE animals (Fig. 1f). Similarly, in the VPA-exposed animals, smaller spines were associated with spine elimination, and the rate of the elimination was twice as high as that in UE animals (Fig. 1g).

Newly generated spines clustered more frequently in VPA-exposed marmosets than in controls

The generation of spines in close proximity, or clustered spine generation, is considered to have functional significance, especially in learning and memory[7, 14, 34, 35]. We next examined whether the generated and eliminated spines in the VPA-exposed and UE marmosets were clustered or not (Fig 2a). We chose a 3-μm window for our analyses, since a number of biochemical, physiological, and structural studies have suggested that a 3- to 10-μm distance between spines facilitates sharing of resources, spine co-activation, and learning-induced structural plasticity[42-47]. Clustered spine generation occurred much more frequently (4.4-fold) in the VPA-exposed animals than in the UE animals (Fig. 2b), even though the total number of spine occurrences in the VPA-exposed marmosets was only about twice as large as in the UE marmoset (Fig. 1d). Clustered spine elimination was also more common in VPA-exposed marmosets than in UE marmosets, although not statistically significant (Fig. 2b). The difference in the clustered spine elimination was only 2.5-fold, which is approximately the same magnitude (2-fold) as for overall spine elimination (Fig. 1d). Next, we created a cumulative plot of the distance between generated spines and between eliminated spines. As shown in Fig. 2c and 2d, there was a significant difference in the distribution of interspine distances between the VPA-exposed and UE groups in both generated and eliminated spines. Again, the difference between the VPA-exposed and UE animals in terms of the probability of clustered spine generation was large (2.8 fold; Fig. 2c), while that of clustered spine elimination was small (1.4 fold; Fig. 2d). These results suggest the existence of a mechanism by which dendritic spines actively appear in clusters in the animals exposed to VPA. Therefore, we conducted a Monte Carlo simulation experiment to determine whether there was more clustering bias in VPA-exposed marmosets than in the hypothetical uniform random spine distribution (Fig. 2e). The distribution of the probability of cluster formation after 30,000 simulation trials is shown in Fig. 2f–i by the gray connected lines. The actual clustering probabilities are indicated by the arrows. The clustering probability of the

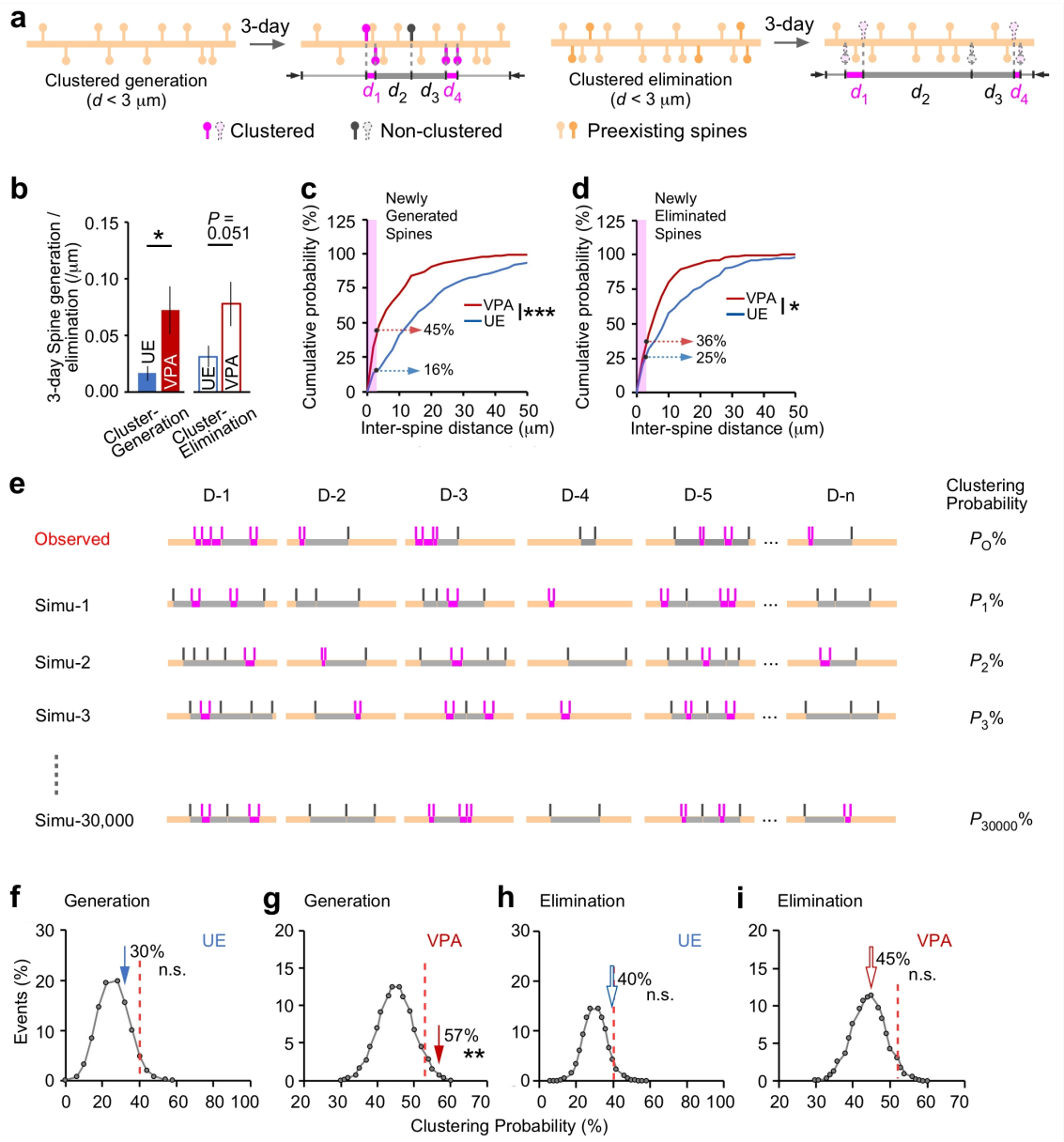

182 generated spine pair was approximately twice as high in the VPA-exposed group (57%) than in
183 the UE group (30%). In addition, the clustering probability of the generated spine pairs was
184 greater than the 95th percentile of the simulation distribution in the VPA-exposed group (Fig. 2g),
185 but remained below the 95th percentile in the UE group (Fig. 2f). The clustering probabilities of
186 the eliminated spine pairs did not exceed the 95th percentile in either the UE group (Fig. 2h) or
187 the VPA-exposed group (Fig. 2i). We conclude that the clustering of newly generated spines, but

Fig. 2 Dendritic spine clustered generation is more predominant than clustered elimination in VPA-exposed marmosets. **a** Schematic drawing of clustered spine generation (left panel) and elimination (right panel). Pairs of newly generated or eliminated spines were considered to be clustered if they occurred within 3 μm of each other. Spines colored magenta or gray represent clustered and non-clustered spines, respectively. **b** Comparison of the density of clustered generated spines between UE and VPA-exposed animals (mean ± s.e.m.; $P = 0.016$, Mann-Whitney U test; $n = 14$ and 12 dendrites in four and three UE and VPA-exposed animals, respectively; left panel), and the density of clustered eliminated spines (right panel). **c, d** Distribution of inter-spine distances between newly generated spines (c) ($P = 0.0009$; Kolmogorov-Smirnov test; n = 45 and 85 spine pairs in UE and VPA-exposed animals, respectively) and between newly eliminated spines (d) ($P = 0.013$; $n = 69$ and 101 spine pairs in UE and VPA-exposed animals, respectively). Magenta-shaded areas indicate inter-spine distances shorter than 3 μm, and numbers indicate the probabilities of clustering within 3 μm. To prevent underestimation of the inter-spine distance, a resampling method was used. See Methods for details. **e** Validation of clustering bias by Monte Carlo simulation. In the simulation, the new spine positions were randomly determined with a uniform distribution without changing the spine number or length and number of each dendrite. Clustering probabilities for all inter-spine distances were calculated for each simulation, and the distributions of the clustering probability from 30,000 iterations are shown in (f)-(i). f-i Circles connected with gray lines represent probability plots of clustering events from 30,000 simulations; the actual numbers of spine clusters are represented by arrows ($P = 0.30$ and 0.006; $n =$ 23 and 65 newly generated spine pairs in 14 and 12 dendrites in UE and VPA-exposed animals, respectively) ($P = 0.0503$ and 0.37; $n = 43$ and 78 newly eliminated spine pairs in 14 and 12 dendrites in UE and VPA-exposed animals, respectively). Dotted red lines show 95th percentiles. See Methods for details. $^{***}P < 0.001$; $^{**}P < 0.01$; $^{*}P < 0.05$; n.s., not significant.

not of eliminated spines, in the dendrites of VPA-exposed marmosets is enhanced rather than randomly distributed.

The carryover fraction of newly generated spines was higher in VPA-exposed marmosets than in controls

The neuronal turnover rate supposedly represents the pace of change in the neural circuitry. However, the turnover rate alone does not provide information on how long the effects of circuitry changes will persist. Three consecutive imaging sessions allowed us to monitor the fate of pre-existing and newly generated spines over 3 days[16]. The carryover fraction was defined as the fraction of newly generated spines that survived to the last session (Fig. 3a, b, GS). The carryover fraction was two times higher in VPA-exposed marmosets than in UE marmosets (Fig. 3c). This suggests that experience-induced changes in spines may be more likely to persist in VPA-exposed marmosets. We further divided the newly generated spines into clustered and non-clustered spines and computed their carryover fractions. The carryover fraction of clustered spines in VPA-

exposed marmosets was six times higher than that in UE marmosets (Fig. 3d). On the other hand, there was no difference in the carryover fraction of non-clustered spines with or without VPA treatment (Fig. 3d). Thus, clustered emerging spines were predominant in the carryover of generated spines in the model marmosets.

Having analyzed the collective nature of spines, we next analyzed the temporal stability of individual spines. Spine stability was defined as the percent ratio of newly generated or pre-existing spines that survived to the last session. Both in the VPA-exposed and UE groups, the spine stability of newly generated spines (~50%) was considerably lower than that of pre-existing spines (~90%) (Fig. 3e). However, the spine stability of these two types of spines did not differ between the VPA-exposed and UE groups (Fig. 3e). Furthermore, spine stability in both the VPA-exposed and UE groups was independent of the presence or absence of clustering (Fig. 3f). The fact that spine stability was the same regardless of clustering suggests that interactions among newly formed spines have little effect on spine stability after a sufficient time has elapsed since spine generation. In summary, clustered carryover spines comprised a much higher proportion of total spines in the VPA-exposed marmosets than in the UE animals, while the stability of individual spines was equivalent in the two groups.

Axonal boutons had a higher turnover rate in VPA-exposed marmosets than in controls

Deficits in projection-specific connectivity or cortical interaction have often been discussed in ASD, as exemplified by local overconnectivity and long-range underconnectivity[48, 49]. Spine turnover may depend on which neuron the coupled axons originate from[15]. We next analyzed marmoset axons that were transfected with differently colored fluorescent proteins depending on the dmPFC hemisphere from which they projected (Fig. 4a). We expressed red fluorescent protein in neurons ipsilateral to the observation window in the PFC, and green fluorescent protein in

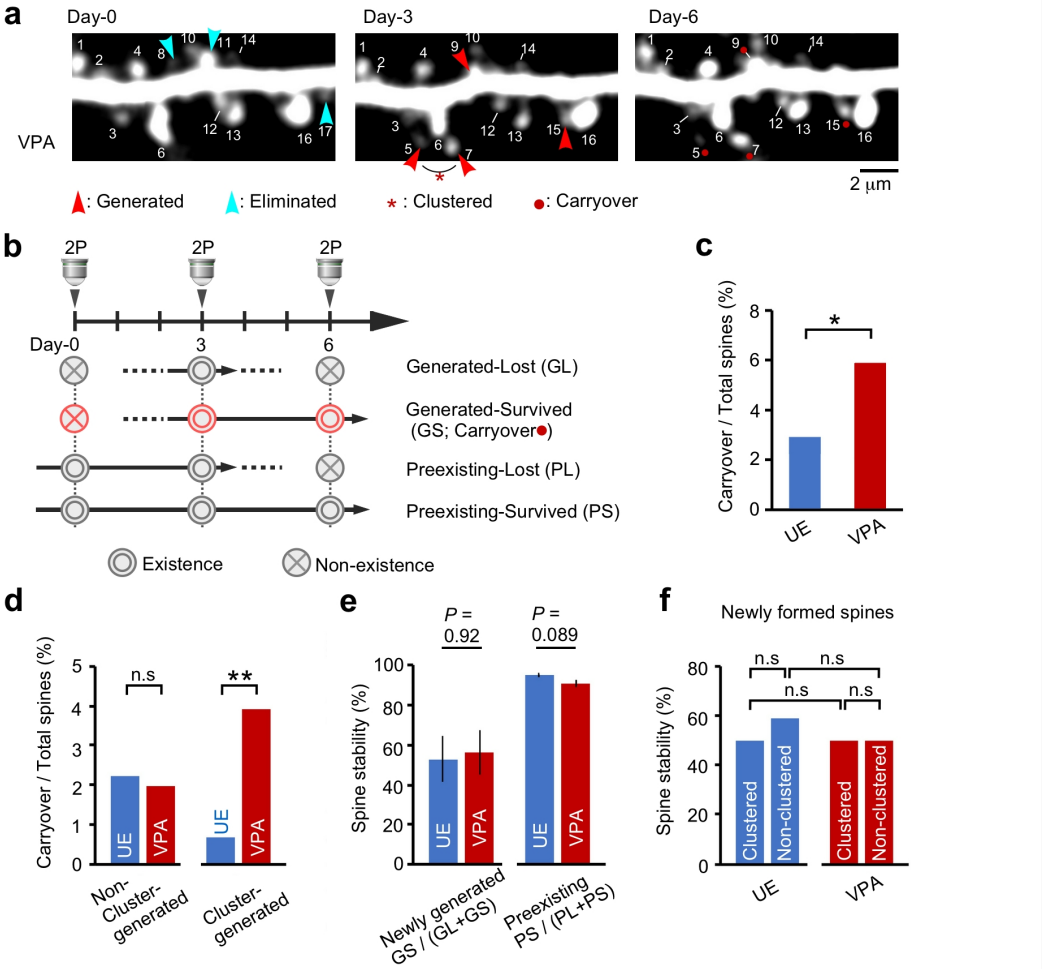

Fig. 3 The surviving fraction of newly generated spines (carryover spines) was much larger in VPA-exposed marmosets than in controls, although the survival rate of each spine did not differ. **a** Representative dendrite images taken every 3 days are presented as in Fig. 1b. **b** A diagram showing four patterns of spine generation and elimination. The red dot in the legend indicates the carryover spines labeled with a red dot in Figs. 1b and 3a. **c** The ratio of the surviving fraction of newly formed spines (carryover spines) to the total spines was larger in VPA-exposed animals than in UE animals. (P = 0.046; Pearson's Chi-square test; n = 13, 448, 21, and 357 for UE carryover spines, UE total spines, VPA-exposed carryover spines, and VPA-exposed total spines, respectively). **d** Among clustered spines, the ratio of the carryover spine fraction to the total spines was much larger in VPA-exposed animals than in UE animals (P = 0.0018; Pearson's Chi-square test; n = 3, 448, 14, and 357 for UE carryover, UE total, VPA-exposed carryover, and VPA-exposed total spines, respectively). By contrast, the carryover spine fraction was not significantly different among non-clustered spines (P = 0.79; Pearson's chi-square test; n = 10, 448, 7, and 357 for UE carryover, UE total, VPA-exposed carryover, and VPA-exposed total spines, respectively). **e** The survival rate of each newly generated and pre-existing spine was not significantly different between UE and VPA-exposed animals (mean ± s.e.m.; Mann-Whitney U test; n = 11 and 10 (newly generated), and 13 and 11 (pre-existing) dendrites from three and three UE and VPA-exposed animals, respectively). f The survival rate of each newly formed spine was not significantly different between the clustered and non-clustered spines (P > 0.99; Fisher's exact test; n = 3,10, 3, and 7 for clustered GS, non-clustered GS, clustered GL, and non-clustered GL spines, respectively, in UE animals) (P > 0.99; Fisher's exact test; n = 14,7, 14, and 7, respectively, in VPA-exposed animals). **P < 0.01; *P < 0.05; n.s., not significant.

228 neurons on the contralateral side of the brain (same axial position, and same distance from the

midline; See **Methods** section; Fig. 4a). Therefore, we were able to observe red dendrites and red axons from local neurons, as well as green axons from contralateral neurons (Fig. 4b). In the magnified images, varicosities called presynaptic boutons were seen on the axons; new generation and elimination of these varicosities were seen on each of the 3 observation days (Fig. 4c). Previous studies have shown that these boutons constitute pre-synapses[50], although some synapses apparently lack boutons. Most boutons in our sample were en passant boutons, and there were relatively few terminal boutons with a neck between a varicosity and a parental axon shaft (Fig. 4c). We considered the boutons to represent the existence of pre-synapses in the present study. We first measured the axonal bouton density and found a significant difference between the mean values of the ipsilateral and contralateral UE marmoset axons. By contrast, the difference between the ipsilateral and contralateral axons in VPA-exposed marmosets was not significant (Fig. 4d). Next, we calculated the bouton size under the assumption that it was proportional to the maximum fluorescence intensity, and found that the distribution of bouton size was almost identical between the VPA-exposed and UE groups (Fig. 4e). We then calculated the 3-day bouton generation and elimination rates. Consistent with the rates of spine generation and elimination, those of bouton generation and elimination were higher in VPA-exposed animals (Fig. 4f). Detailed analysis of each type of axon showed a significant difference in ipsilateral bouton gain between the two groups, whereas there was no significant difference in contralateral bouton gain (Fig. 4g). This suggested that the difference in the generation and elimination of synapses between the VPA-exposed and UE groups may have been caused by the alteration of ipsilateral axons. The 3-day bouton turnover rate was much larger than the spine turnover rate (spine: 10.2% and 12.6% for VPA-exposed group, 5.2% and 7.8% for UE group, for generation and elimination, respectively). We set the bouton threshold as twice the thickness (brightness) of the axon shaft. Since we do not detect axonal synapses below the bouton threshold, the subthreshold boutons can be misidentified as newly generated boutons when they enlarge and exceed the threshold. As a consequence, the number of newly generated boutons can be

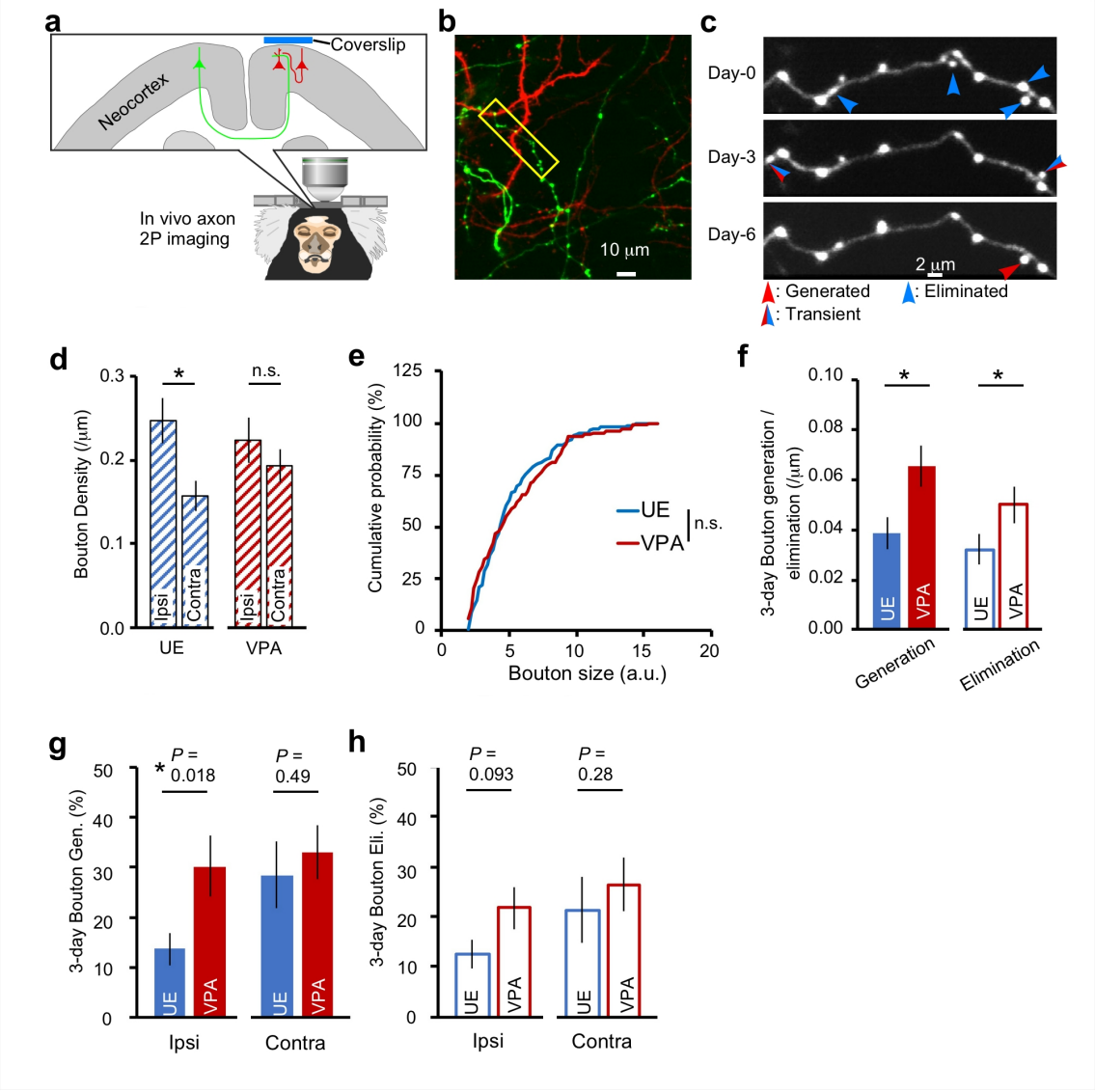

overestimated. Likewise, the number of boutons that are eliminated can be also overestimated. Although including such overestimations, the results presented here are the first results showing that synaptic turnover varies with the cortical origin of the input. Abnormalities of diverse brain connectivity in ASD have been demonstrated by functional brain imaging techniques such as functional magnetic resonance imaging (fMRI) and magnetoencephalography (MEG) / electroencephalography (EEG), using the degree of brain activity coherence as an indicator[1, 48, 49]. Our finding of divergent plasticity in local and long-distance connections in VPA-exposed animals introduces a new dimension to projection-specific variation in ASD. Mismatch in plasticity control involving local and long-range connections may contribute to autonomous local

Fig. 4 Two-photon in vivo axon imaging in ASD model marmosets. a AAV vectors expressing different colored fluorescent proteins were inoculated into each hemisphere of the dmPFC. **b** Axons from the contralateral hemisphere had green fluorescence, and axons from the ipsilateral hemisphere and dendrites had red fluorescence. **c** A representative axon from a VPA-exposed animal (the axon surrounded by the yellow rectangle in (b)) was imaged every 3 days. **d** Mean bouton densities are significantly larger in ipsilateral axons than in contralateral axons in UE animals (P = 0.035, Mann-Whitney U test; n = 28 and 21 ipsilateral and contralateral axons, respectively, from three animals). They are not significantly different between ipsilateral and contralateral axons in VPA-exposed animals (P = 0.36, Mann-Whitney U test; n = 22 and 25 ipsilateral and contralateral axons, respectively, from two animals). The mean densities of terminal boutons were much lower than those of en passant boutons in our sample (mean terminal bouton density: 0.023, 0.012, 0.021, and 0.010 boutons/μm for UE ipsilateral, UE contralateral, VPA-exposed ipsilateral, and VPA-exposed contralateral axons, respectively). **e** The bouton size distribution between these animals (P = 0.57; Kolmogorov-Smirnov test; n = 149 and 107 boutons and 49 and 47 axons in three and two UE and VPA-exposed animals, respectively). **f** There is a significant difference in the mean bouton generation per unit length between these animals (P = 0.012, Mann-Whitney U test; n = 49 and 47 axons in three and two UE and VPA-exposed animals, respectively), and also in 3-day bouton elimination (P = 0.043). **g, h** Three-day mean bouton generation (g) and elimination (h) percentages for each axon type are shown (mean ± s.e.m.; Mann-Whitney U test) (n = 28, 22, 21, and 25 for UE ipsilateral, VPA-exposed ipsilateral, UE contralateral, and VPA-exposed contralateral axons, respectively). The mean bouton turnover rates were higher than those of spines (5.2%, 10.2%, 7.8%, and 12.6% for UE generation, VPA-exposed generation, UE elimination, and VPA-exposed elimination of spines, respectively). *P < 0.05; n.s., not significant.

circuit remodeling without regard for the highly contextualized information computed in the brain-wide global network.

Oxytocin nasal administration modified dendritic spine clustering

Clinical trials on oxytocin in humans are currently inconclusive[22-25]. In order to better understand the clinical applications of oxytocin, it is therefore important to investigate its mechanism of action on synaptic phenotypes, which were characterized in this study in VPA-exposed marmosets. Thus, we next examined how the aforementioned properties of cortical synapses changed after the administration of oxytocin, which has been reported in some studies to be effective in treating the core symptoms of ASD. Marmosets were administered saline and then oxytocin intranasally, in the manner described in the **Methods** section (Fig. 5a). The average results from all marmosets failed to show a significant effect of oxytocin on spine generation and elimination, although a monotonically increasing trend of non-clustered spine generation and elimination was observed (Fig. 5b, c). Thus, we next examined the effect of oxytocin

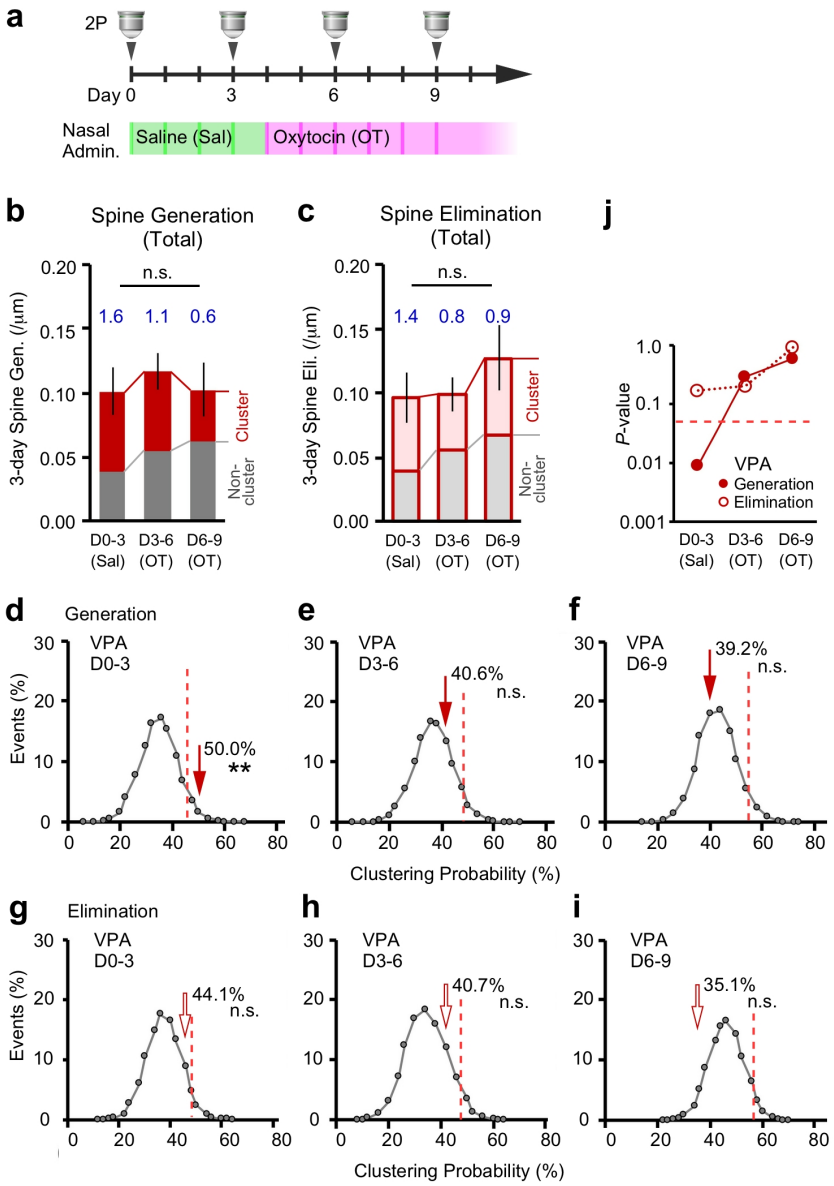

Fig. 5 Oxytocin modifies the proximity of spine generation in the model marmosets. a A schema of oxytocin nasal administration and two-photon (2P) imaging. Saline was given to marmosets in the green-shaded period, while oxytocin was given in the magenta-shaded period (See Methods for details). **b, c** Mean values of 3-day spine generation (b) and elimination (c) are not significantly different before and after oxytocin administration. (mean ± s.e.m.; $P = 0.25$ and $P = 0.62$ for spine generation and elimination, respectively, Friedman test; $n = 12$ dendrites in three VPA-exposed animals). The blue numbers indicate the ratio of clustered to non-clustered spines. **d–i** Effects of oxytocin on clustering bias of newly generated (d–f) and eliminated (g–i) spines. The graphs are shown as in Figs. 2f-i. ($n = 32$, 32, and 28 newly generated spine pairs and n = 34, 27, and 37 newly eliminated spine pairs during the D0–3, D3–6, and D6–9 periods, respectively, in three VPA-exposed animals). **j** The *P*-values expressed in logarithm from (d)–(i) are indicated. The red dotted line indicates 0.05. $^{**}P < 0.01$; n.s., not significant.

278 administration on spine clustering (Fig. 5d–j). Unexpectedly, the proximity between generated

279 spines observed in VPA-exposed animals (Fig. 2g) during saline administration, was alleviated

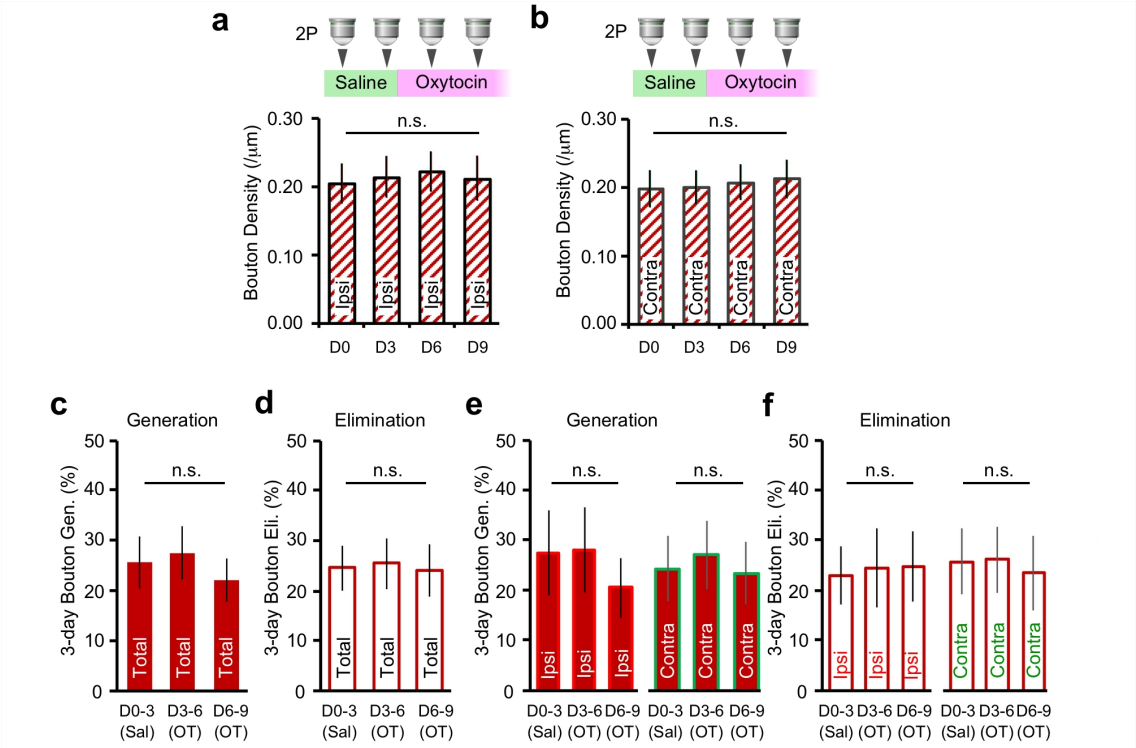

Fig. 6 Oxytocin does not significantly modify axonal bouton generation or elimination. a, b Mean bouton density values of ipsilateral (a) and contralateral (b) axons in VPA-exposed animals are not significantly different before and after oxytocin administration. (mean ± s.e.m.; $P = 0.997$ and $P = 0.898$ for ipsilateral and contralateral axons, respectively, Kruskal-Wallis test; $n = 17$ and 21 for ipsilateral and contralateral axons, respectively) **c, d** Three-day bouton generation (c) and elimination (d) during the D0–3, D3–6, and D6–9 periods for each axon type are shown (mean ± s.e.m.; $P = 0.85$ and $P = 0.96$ for bouton generation and elimination, respectively, Kruskal-Wallis test; n = 38 axons in two VPA-exposed animals). **e, f** Three-day bouton generation (e) and elimination (f) during the D0–3, D3–6, and D6–9 periods for the total axons in the VPA-exposed animals are shown as in (c, d) (mean ± s.e.m.; $P = 0.85$ and $P = 0.97$ for ipsilateral and contralateral bouton generation, respectively, $P = 0.99$ and $P = 0.91$ for ipsilateral and contralateral bouton elimination, respectively, Kruskal-Wallis test; $n = 17$ and 21 ipsilateral and contralateral axons in two VPA-exposed animals). n.s., not significant.

by nasal oxytocin administration (Fig. 5d–f, j). By contrast, oxytocin had a less pronounced effect on the proximity between eliminated spines (Fig. 5g–i, j).

We next analyzed the effect of oxytocin on axons. The bouton density, generation, and elimination of each axon species were not significantly different before and after oxytocin administration (Fig. 6a–f).

Gene expression analysis in adult ASD model marmosets

To explore the molecular mechanisms of abnormal spine dynamics in VPA-exposed marmosets and to assess the validity of adult VPA-exposed marmosets as a model of idiopathic ASD, we performed transcriptome analysis of the cerebral cortex using custom-made marmoset microarrays. Among 9,296 genes expressed in the cortical tissues, there were 2,484 differentially expressed genes (DEGs) with an adjusted p-value for multiple comparison (P_{adj}) of < 0.05. First, we compared the DEGs in the cortical regions associated with social behavior between VPA-exposed marmosets and the postmortem brains of humans with ASD, and found a significant positive correlation between the two groups[31] (Fig. 7a). This was similar to the property we had previously reported in juvenile VPA-exposed marmosets[11]. In addition, the modulation of gene expression in adult marmoset models and in human ASD was compared in each gene module that was previously configured by weighted gene co-expression network analysis (WGCNA) for typically developed and ASD human samples[11, 31]. In both the marmoset model and human ASD, the majority of genes in modules associated with neurons and oligodendrocytes were downregulated (Fig. 7b), while genes in modules associated with astrocytes and microglia were upregulated (Fig. 7b). The direction of gene expression modulation of adult VPA-exposed marmosets was significantly similar to that of human ASD samples in 10 modules, one module greater than that of juvenile VPA-exposed animals[11] (Fig. 7c). Note that the human ASD transcriptomes that were analyzed were derived from individuals of various ages, from children to adults. The high similarity between VPA-exposed marmosets and human ASD contrasts with the representative rodent monogenic ASD models, which replicated human modulations only in limited gene modules and cell types (Fig. 7c). One explanation for this may be that these transgenic mice are a model of a specific type of ASD in which one gene contributes particularly strongly, which is not the case in idiopathic ASD. We further confirmed that the correlation between the transcriptome of the macaque MeCP2-Tg model and that of human ASD was low (Fig. 7d).

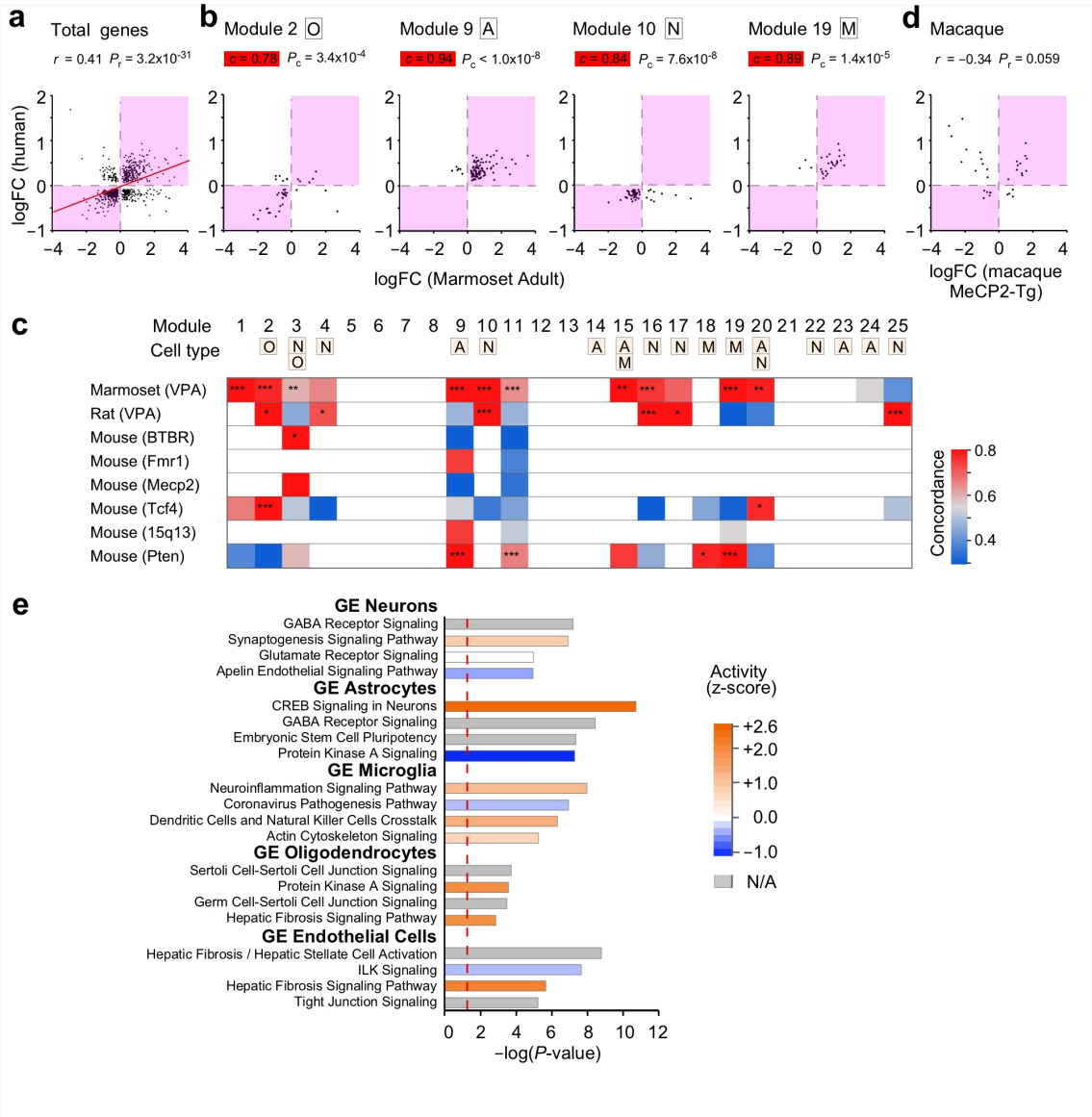

We also analyzed DEGs in each cell type. This analysis confirmed the presence of a VPA-exposed marmoset–specific phenotype across the four cell types, as well as in vascular endothelial cells in the brain (Fig. 7e). Pathway analysis of cell type–specific DEGs showed pathway abnormalities in each of these cell types. For example, microglial modules exhibited abnormalities associated with inflammation, which fits well with the inflammation hypothesis of ASD[51].

Fig. 7 Gene expression modulations in adult marmoset social neocortical areas reflect those in human ASD as determined by microarray analysis. **a, b, d** Relationship of gene expression modulation between adult marmosets and postmortem samples from humans with ASD (a, b), and between a MeCP2-Tg macaque model and human ASD (d). As a measure of gene expression modulation, log fold-change (logFC) values were computed between ASD model animals and control animals, and then compared with human ASD data. Modulated genes with $P_{adj} < 0.1$ are plotted. Pearson's correlation coefficient (r) and the P-values for the correlation coefficient (P_r) was shown in (a) and (d). As a measure of concordance in the direction of gene expression modulation, two-sided P-values for concordance (P_C) are shown in (b). The magenta-shaded areas represent the first and third quadrants, indicating that the two elements have changed in the same positive or negative direction. The red line in (a) is the linear regression. See Methods section and Supplementary Methods file for detailed procedures. **c** Concordance of gene expression modulations across human modules. The color indicates concordance between animal model and human ASD modules with at least eight genes in common. Asterisks represent P-values determined using the one-sided binomial test: $^{*}P < 0.05$, $^{**}P < 0.01$, $^{***}P < 0.001$. Precise information for obtaining the concordance between human and model animals other than the adult VPA-exposed marmosets were described in Supplementary Methods. For the rat VPA-exposed model and BTBR mice, genes with $P_{adj} < 0.05$ were selected; for other models and human ASD, those with $P_{adj} < 0.1$ were selected. **e** Enriched pathways for each cell type. The genes most closely associated with neurons, astrocytes, microglia, oligodendrocytes, and endothelial cells were analyzed. The color of the bars represents the direction of regulation of the pathway based on the logFC values. The p-values of enrichment were provided by the IPA software. The red dotted line represents the significance threshold ($P = 0.05$).

Discussion

In this study, we used in vivo two-photon imaging to monitor synaptic dynamics in the apical tufts of layer 2/3 pyramidal neurons in the dmPFC of VPA-exposed marmosets, an improved model of idiopathic ASD. This study resulted in several important findings (Fig. 8a). (1) Synaptic turnover was enhanced in VPA-exposed marmosets. (2) Newly generated spines actively formed clusters in the model marmosets. (3) These animals also had a higher carryover of generated spines. The difference was particularly large for clustered spines. These results suggest that there are maladjustments of synaptic updating and inter-synaptic interaction in VPA-exposed marmosets. Finally, (4) nasal administration of oxytocin to model marmosets reduced the tendency of spines to cluster without affecting their turnover rate. These synaptic effects of oxytocin may underlie its therapeutic potential in individuals with ASD.

ASD model mice that have thus far been examined by in vivo two-photon microscopy showed higher spine dynamics as a common phenotype in motor cortices and early sensory areas, which

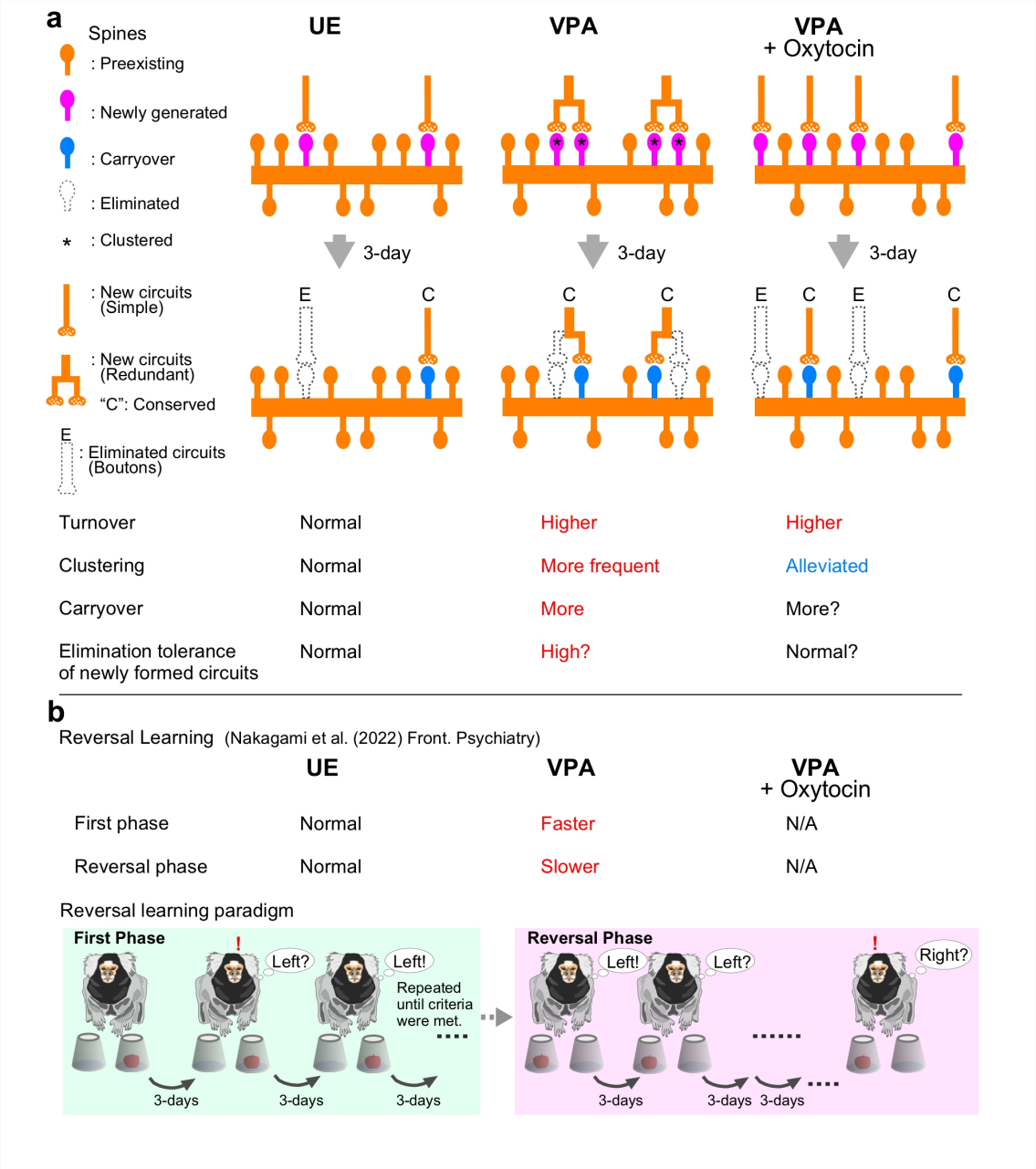

335 are less associated with ASD core symptoms than the PFC[13-17]. These mice comprise diverse
336 genetic alteration models and inbred BTBR strains. Accumulating evidence, including the results
337 of the current study, suggests that ASD-related genes and environmental factors may converge
338 across species and result in the phenotype of increased spine dynamics, suggesting ongoing
339 enhanced remodeling of neural circuits. In human adults with ASD, the PFC tends to have
340 elevated levels of N-acetyl aspartate (NAA), a metabolite indicating neural activity[52]. This
341 phenotype could be related to the increased spine turnover that is associated with neural activity.

Fig. 8 Schematic drawing of the effects of spine dynamics in VPA-exposed model marmosets. a An overview diagram illustrating how redundantly generated spines may provide circuit stability. In VPA-exposed marmosets, there were approximately two times more newly generated spines (magenta) than in UE marmosets. More generated spines were clustered (asterisk; 4.4 fold) and survived for 3 days (blue; carryover spines; 5.9 fold) in the VPA-exposed animals than in the UE animals. The clustered generated spines are expected to form functionally redundant neural circuits (likely with local axons) that are resistant to random spine erasure ("C" in the figure shows the conserved circuits). This model suggests that learning effects may last longer in VPA-exposed marmosets, and may be difficult to erase. The clustering was alleviated by oxytocin administration, which may increase the flexibility of the circuit. The elimination of pre-existing spines and axons are omitted from the diagram for clarity. The figure key is shown in the upper left. **b** The above model for circuit reconfiguration in VPA-exposed marmosets may explain the following features of reversal learning in the ASD-model animals. In the previous study, our group performed an operant task and its reversal paradigm (30). In the first discrimination phase of the paradigm, a marmoset learned to obtain a hidden reward, which is consistently placed on the left or right side of two options every 3 days. Once the success rate reached the specified criterion, the reward was moved to the opposite side beginning in the next session, and the marmoset continued to engage in the task. The VPA-exposed marmosets learned faster in the first phase and slower in the reversal and re-reversal phases than the UE animals.

In our study, the newly generated spines in the basal state tended to cluster, and these clustered spines exhibited a high carryover rate in the ASD model marmosets. The clustering in synaptic plasticity is often discussed in the context of learning and memory[35, 53]. CCR5 KO and MeCP2 duplication mice commonly exhibit elevated spine turnover and clustering, as well as higher learning efficiency[14, 34]. On the other hand, FMR1 KO mice show lower learning efficiency with increased spine turnover but no clustering of generated spines[16, 54]. Consistent with these findings, our group previously showed that VPA-exposed marmosets learned faster than UE marmosets during the first discrimination phase of a spatial reversal learning task (Fig. 8b)[30].

The process by which co-activated spines are formed in proximity to each other during an operant task was recently elucidated using the combination of a behavioral task and functional two-photon imaging[7]. According to an electron microscopy study, adjacent spines often serve as postsynaptic targets of single axons[55]. In layer 2/3 pyramidal neuron dendrites of the ferret visual cortex, neighboring spines tend to have similar visual representations[56]. Clustered generated spines, due to their redundant involvement in the circuit, may help stabilize the formed circuit and

358 accelerate learning[57]. At the same time, however, they may overstabilize the circuit and thereby
359 compromise its flexibility. This is more likely in VPA-exposed marmosets, which exhibited no
360 significant clustering tendency in terms of spine disappearance (Fig. 8a). Interestingly, the VPA-
361 treated marmosets in the study[30] had a slower learning rate during the reversal phase of the
362 reversal learning task (i.e., after paradigm reversal) (Fig. 8b). Note that in the particular reversal
363 learning task for analyzing mid-term (days to weeks) cognitive inflexibility, the training interval
364 between sessions was set at ~3 days, which was close to the interval used in our two-photon
365 microscopy experiments[30] (Fig. 8b). We propose that a similar phenotype of spine dynamics
366 might contribute to the superior memory of individuals with ASD and their adherence to habits
367 formed without apparent training. However, further research is needed to test this hypothesis.
368
369 In this study, oxytocin reduced the clustering of emerging spines without altering spine
370 turnover in ASD model marmosets (Fig. 8a). Although there are studies on the effects of oxytocin
371 on synaptic plasticity[18, 20], its impact on spine clustering is unexpected, indicating the possibility
372 that spine turnover and clustering can be controlled separately. This effect of oxytocin could
373 restrain excessively prolonged circuit stability and mitigate behavioral perseverance, as reported
374 in human ASD[58]. In fact, oxytocin reduced the levels of metabolites of excitatory
375 neurotransmitters in the PFC of humans with ASD[59]. A mouse model of major depression also
376 demonstrated a relationship between treatment effects on symptoms and changes in clustered
377 spine dynamics[36]. It remains to be tested whether oxytocin can improve the low performance in
378 the reversal phase in VPA-exposed marmosets (Fig. 8b). Differences in oxytocin systems between
379 rodents and primates may significantly affect therapeutic efficiency, which underscores the
380 importance of primates in translational research on oxytocin[32]. For instance, oxytocin receptors
381 are rarely expressed in the primate cortex[32, 60]. This contrasts with rodents, in which oxytocin
382 receptors are enriched in various cortices, including the medial PFC. In the PFC, oxytocin may
383 preferentially bind to vasopressin receptors, which are relatively abundant in the primate cortex[32,

384 [60]. Another characteristic of primates is that the cholinergic system in the basal forebrain, which
385 projects throughout the cortex, is enriched in oxytocin receptors, a feature not found in rodents[60].
386 The pathway by which oxytocin influences cortical synaptic dynamics in VPA-exposed
387 marmosets remains an important open question.
388
389 To identify therapeutic targets, it would be valuable to determine the molecular mechanisms[61]
390 that govern synaptic turnover and spine clustering in VPA-exposed marmosets. The spine
391 clustering in the MeCP2 duplication mouse model was suppressed by an inhibitor of Ras–ERK
392 signaling without altering the spine generation rate[62]. Ras, like other proteins such as Rho, Rac,
393 and cofilin, has been reported to diffuse from activated spines to neighboring spines via dendrites
394 and is thought to alter the plasticity of neighboring spines[7, 43, 45, 63]. Interestingly, transcriptome
395 analysis of our model marmosets showed two-fold higher upregulation of TrkB (NTRK2), which
396 is upstream of the Ras–ERK pathway. Synaptic plasticity involves not only neurons but also
397 diverse glial cells. We found that microglia demonstrated activation of signals related to viral
398 infection, inflammation, and reorganization of the actin cytoskeleton (Fig. 7d). Suppression of
399 excessive microglial activation with minocycline or other matrix metalloproteinase-9 inhibitors
400 has been reported to suppress excessive spine turnover in fragile-X model mice[17]. Our
401 transcriptomic analysis also revealed significant down-regulation of diverse myelin-related genes
402 (such as *MBP*, *PLP1*, and *MOBP*) that suppress heightened cortical plasticity, even during the
403 critical period of the rodent visual cortex development (See **Supplementary Data 1**).
404 On the other hand, enhanced synaptic remodeling may be caused not only by alterations in the
405 innate properties of central nervous tissues, but also by aspects of the brain environment. For
406 example, it has been shown that the stress hormone corticosterone increases synaptic turnover in
407 mice[64]. Indeed, as in mouse ASD strains[65] and humans with ASD[66], our ASD model marmosets
408 have aberrant cortisol responses[67], suggesting that anxiety and disorders of the endocrine system
409 could be responsible for the increase in synaptic remodeling.

In this study, we demonstrate novel features of spine dynamics in adult ASD model marmosets, and suggest these features as a potential therapeutic target in ASD. Our previous study has shown that an imbalance between circuit remodeling and consolidation also occurs in young VPA-exposed marmosets, including changes in long-term depression (LTD) and reduced expression of critical period–related genes[11]. However, we also acknowledge that particular phenotypes associated with synapse and related gene expression domains continue to change as individuals grow. For example, LTD abnormalities in infant marmosets are far less evident in more grown child marmosets[11]. Atypical gene expression in model marmosets is concordant with that in human ASD in a higher number of modules in their adulthood than in childhood (Fig. 7c). A more detailed comparative study of the ASD model marmosets in childhood and adulthood should provide deeper insights into age-dependent precision medicine.

Methods

Animals

All experimental procedures were approved by the Animal Research Committee of the National Center of Neurology and Psychiatry. Common marmosets (*Callithrix jacchus*) were housed in captivity at the National Center of Neurology and Psychiatry under a 12-h/12-h light/dark cycle and were fed food (CMS-1; Clare Japan) and water ad libitum. Temperature was maintained at 27–30°C and humidity at 40–50%.

Marmoset ASD model

Serum progesterone levels in female marmosets were regularly measured to determine the date of fertilization. Four percent VPA dissolved in 10% glucose solution was administered intragastrically to pregnant marmosets at 200 mg/kg/day daily for 7 days starting on gestation day 60. No doses were given to control mothers. The obtained ASD model offspring from VPA-

administered mothers and control offspring from UE mothers were kept in their home cages until the day of inoculation with AAV vector. We used four UE marmosets (monkeys KR (f, 1.3), TR (f, 3.2), VR (m, 2.2), and BH (m, 1.3)) and three VPA-exposed marmosets (monkeys PR (f, 1.5), SH (f, 1.4), and MS (m, 1.3)); f or m and numbers in parentheses indicate sex and age in years at the time of AAV inoculation, respectively.

AAV vector inoculation of the marmoset neocortex

Each experimental marmoset was pretreated with the antibiotic cefovecin sodium (8 mg/kg body weight, intramuscular (i.m.); Zoetis), prednisolone (2 mg/kg body weight; i.m.), the analgesic ketoprofen (2 mg/kg body weight, i.m.), and atropine (0.15 mg/kg body weight, i.m.). It was then anesthetized with ketamine (15 mg/kg body weight, i.m.; Daiichi-Sankyo) and xylazine (1.2 mg/kg body weight, i.m.; Bayer), which were supplemented with sevoflurane inhalation (2–4%). The marmoset was then fixed to a stereotaxic instrument (SR-6C-HT; Narishige, Tokyo, Japan). During all surgical procedures, marmosets were also supplied with humidified oxygen as needed, and warmed to 37–39 °C with a heating pad (FST-HPS; Fine Science Tools, North Vancouver, Canada). Body temperature, SpO_2, heart rate, cardiac electrogram, respiratory rate, and actual concentration of oxygen and sevoflurane were measured using a biomonitor (BSM-5132; Nihonkoden, Tokyo). After incision of the skin at the midline, the skull was exposed and a 1-mm-diameter hole was made bilaterally above the PFC Brodmann area 8 (11.5 mm anterior to the interaural line, 3 mm lateral to the midline) using a dental drill.

A puller (PC-100; Narishige) was used to create a micropipette (tip diameter 30–50 μm) from a micro glass tube (1.0-mm diameter; TW100F-4; WPI, USA). The pulled micropipette was then beveled using a micro grinder (EG-402; Narishige) and was sterilized by overnight exposure to UV light or ethylene oxide. The pipette was set to a glass microsyringe (Model 1701,10 μL; Hamilton, USA) using a Priming kit (55750-01; Hamilton), and the microsyringe was back-filled

with silicon oil and attached to a microsyringe pump (LEGATO 130; WPI) fixed to the manipulator of a stereotaxic instrument (SM-15R; Narishige). The micropipette was then tip filled with AAV vector suspension and slowly inserted through the dura and into the neocortex, avoiding large blood vessels. The total 0.5-μL volume of AAV vector was then inoculated at 0.1 μL/min at a depth of 0.8 mm from the surface. The viral preparations were adjusted to the following final concentrations: 1×10^{9} vg/mL for rAAV1-Thy1S-tTA and 1×10^{12} vg/mL for AAV1-TRE3-tdTomato, expressing red fluorescence protein; 5×10^{9} vg/mL for rAAV2/1-Thy1S-tTA and 1×10^{12} vg/mL for rAAV2/1-TRE3-mClover, expressing green fluorescence protein. After the 5-min incubation period, the micropipette was retracted, a silicon plug was stuffed into the cranial hole, and the skin incision was closed with sutures. After recovery from anesthesia, the marmoset was returned to its home cage.

Imaging window preparation

Each experimental marmoset was pretreated with the antibiotic cefovecin sodium, prednisolone, the analgesic ketoprofen, and atropine. It was then anesthetized with ketamine and xylazine, which were supplemented with sevoflurane inhalation (2–4%). The marmoset was then fixed to a stereotaxic instrument. The marmoset was also supplied with humidified oxygen and warmed up to 37–39 °C. After skin incision at the midline, the skull was exposed and a 4-mm-diameter hole was made at the point where the AAV was inoculated using a dental drill fixed to a stereotaxic manipulator (SM-15R; Narishige). The dura mater was carefully removed using microsurgical ophthalmic scissors, fine forceps, and a microhook to minimize any pressure applied to the surface of the brain. A piece of coverslip, consisting of three laminated circular coverslips (5-mm diameter + 3-mm diameter × 2), was used to cover the exposed brain surface[38]. The coverslip was fixed using dental acrylic (Fuji-Lute; GC Corp., Tokyo, Japan) to create an imaging window in the skull. A custom-made stainless-steel recording chamber (ICM, Tsukuba, Japan) was then attached to the skull using dental resin (Bistite II; Tokuyama Dental, Japan) such

that the imaging window was in the center of the chamber. After the imaging window was covered with an acrylic lid, the marmoset was allowed to recover from the anesthesia in the monkey ICU room and was then returned to its home cage.

In vivo two-photon excitation microscopy

In vivo two-photon imaging of neurites was performed using an upright microscope (BX61WI; Olympus) equipped with a laser scanning microscope system (FV1000; Olympus) and a water-immersion objective lens (XLPlanN, 25×, NA 1.05; Olympus). The system included mode-locked, femtosecond-pulse Ti:sapphire lasers (MaiTai; Spectra Physics) set at a wavelength of 980 nm.

Imaging sessions were conducted every 3 days. A marmoset was pretreated with atropine and anesthetized with sevoflurane inhalation (3–5%). The marmoset was laid in the prone position and its head was fixed using the imaging chamber and brass posts (Fig. 1a). In each case, the imaging location was identified based on blood vessel morphology. Tuft dendritic branches (< 100 μm depth) of layer 2/3 pyramidal neurons were used for two-photon imaging experiments. An objective lens correction collar was manually set just before imaging so as to minimize spherical aberrations (i.e., to acquire the brightest image possible). The reciprocal scan mode was used to scan each *xy*-image (256 by 256 pixels; 65 msec/frame). Three-dimensional fluorescent images with 51 *xy*-images, each separated by 0.5 μm, were obtained at each imaging site.

Dendritic spine and axonal bouton analysis

We applied a 2-pixel spatial Gaussian filter and then registered the obtained *xyz*-images using the StackReg or Multi-StackReg plug-in function of Image-J (Fiji)[68]. Spines were identified as protrusions from dendrites with an apparent head structure. Filopodial protrusions (which have no apparent spine head) were excluded from the analysis. Two spines observed during different sessions were considered to represent the same spine if the initial position subsequently exhibited

514 the same distances from adjacent landmarks. A spine was interpreted as lost if it temporarily
515 disappeared. The minimum spine length was set at 0.4 μm. Snowman-shaped spines (shaped like
516 two spheres stuck together) were interpreted as two separate spines. Only spines that appeared
517 laterally were included in the analysis (this underestimated the spine density). Dendrites that were
518 visible in all sessions were used in the analysis.
519
520 We also analyzed the axons that appeared in the same images as the dendrites. For axon analysis,
521 we used five marmosets that expressed mClover in the right hemisphere and tdTomato in the left
522 hemisphere (UE monkeys: TR, VR, BH; VPA-exposed monkeys: SH, MS). We applied a 2-pixel
523 spatial Gaussian filter to the *xyz*-images and obtained *z*-substacked average images for a
524 predetermined z number for each axon. By combining images obtained at the optimal depths, we
525 created montage images for each axon, avoiding dendrites and other axons present at other
526 imaging depths. We then examined the brightness along the axon shaft using the Plot-profile
527 function of Image-J[68]. The ratio of bouton brightness to neighboring axon shaft brightness was
528 then calculated. We did not see axons that were much thicker than the diffraction limit of our two-
529 photon imaging, and discarded areas that overlapped with other dendrites and axons. Boutons
530 were detected as bright swellings along axons, with intensity values at least two-fold higher than
531 that of the flanking axon backbone[69]. The 3-day bouton generation and elimination for unit axon
532 length were obtained by dividing the number of boutons generated and eliminated over a 3-day
533 period by the axon length. The 3-day bouton generation and elimination as a percentage were
534 calculated by dividing the 3-day bouton generation and elimination for unit axon length by the
535 mean bouton density. We did not exclude varicosities of transfer vesicles. In the next session,
536 boutons located within 1 μm of the expected point were interpreted as identical to those in the
537 previous session.
538

The percentage of newly formed spines or boutons was calculated as the number present at time point 2 but not at time point 1, divided by the total number present at time point 1 and multiplied by 100. The percentage of eliminated spines or boutons was calculated as the number present at time point 1 but not at time point 2, divided by the total number present at time point 1 and multiplied by 100.

To prevent underestimation of the inter-spine distances between the newly generated/eliminated spines, inter-spine distances were measured after concatenating all measured dendrites into one long dendrite in Figs. 2c and 2d. The concatenation was repeated 500 times, each time randomly rearranging the order of the dendrites; the average plots of all 500 trials are shown in Figs. 2c and 2d.

Monte Carlo simulation of newly generated or eliminated dendritic spines

Monte Carlo simulation was performed to determine whether a clustering bias exists in the process of spine generation/elimination[34]. We used values obtained from actual measurement for the dendrite number and lengths, and the number of generated/eliminated spines in the simulation. The positions of the generated/eliminated spines on the dendrites were then regenerated with a uniform random distribution using Excel software. The distance between the generated/eliminated spines was computed for all dendrites and the percentage of clustered events was calculated (Fig. 2e). We set the clustering threshold at 3 μm, based on the diffusion distance of calcium ions and molecules along the dendrite shaft[45, 47, 63], and the inter-spine interaction distance of spine plasticity[42]. The above operations were performed 30,000 times to obtain the distribution of clustering events, and the results are shown in Figs. 2f–i and 5d–i by connected gray lines.

Dendritic spine volume measurement

We calculated the spine-head volume by partially summing the fluorescence values of five sequential *z*-images by taking the moving average of the image stack along the *z*-plane. This was done to avoid summing other dendrites or axonal fibers present in different imaging planes. Because the thickness of dendritic spines is near the diffraction limit of a two-photon microscope, partially summed values (2 μm range in the *z*-direction) can be used to reflect spine volumes. Thus, the maximum value of *z*-moving average images allowed us to obtain good approximations of the total *z*-summed stacked images. The normalized spine volume was obtained by dividing the spine fluorescence intensity by the fluorescence intensity of the adjacent dendrite shaft.

Nasal oxytocin administration to VPA-exposed marmosets

New World monkey oxytocin (Pro-8 oxytocin[70]) was custom synthesized (GenScript, Piscataway, NJ, USA) and was dissolved in 0.5 mg/mL of 0.9% NaCl solution. The oxytocin solution was typically administered 2.5 h before the two-photon imaging and at approximately same time on days without two-photon imaging. Oxytocin solution was applied to the nasal cavities of each marmoset at a dose of 150 μg/kg body weight as in a previous study[70], using a micropipette equipped with a soft silicon tube on the tip. Oxytocin was administered every day (monkey MS) or every other day (monkeys PR and SH) starting on day −4 (Fig. 5a). Verification of oxytocin delivery to the cerebral interstitial fluid was verified by measuring the plasma Pro8-oxytocin concentration using a sandwich competitive chemiluminescent enzyme immunoassay (CLEIA) (ASKA Pharma Medical, Fujisawa, Japan). The Pro8-oxytocin concentration in all blood samples was monotonically increased 30 min after nasal oxytocin administration (mean ± s.d. = 30.6 ± 14.8 pg/mL; n = 2 males and 3 females) but not 30 min after nasal saline administration (mean ± s.d. = 9.9 ± 1.7 pg/mL; n = 2 males and 3 females); thus, we concluded that Pro8-oxytocin was successfully delivered to the interstitial fluid of the neocortex.

Microarray gene expression analysis

Microarray analysis of marmoset gene expression was performed using brain samples from three adult VPA-exposed and three UE marmosets, as previously described[11]. To increase data reliability, we pooled the data from the social brain areas (area 12 and area TE) that are affected in humans with ASD. Tissue sampling and GeneChip analysis were conducted as previously reported[11]. Briefly, marmosets were anesthetized with ketamine hydrochloride (50 mg/kg, i.m.) and sodium pentobarbital (90–230 mg/kg, intraperitoneal; Kyoritsu Seiyaku). After reflections had completely disappeared, the animals were transcardially perfused with diethyl pyrocarbonate-treated phosphate-buffered saline, and the cortical tissue was isolated and immersed in RNAlater (Thermo Fisher Scientific). Total RNA was extracted using the RNeasy Mini Kit (Qiagen). RNA integrity was assessed using a Bioanalyzer (Agilent Technologies), and samples with RNA integrity number values >7 were evaluated. Biotin-labeled cRNA probes were prepared using the GeneChip 3'IVT Express Kit (Affymetrix). The probes were hybridized to a custom-made microarray (Marmo2a520631F) using the GeneChip Hybridization, Wash, and Stain Kit (Affymetrix). Microarrays were scanned using a GeneChip Scanner 3000 (Affymetrix) and processed using MAS5, and the reliability of probe detection was examined. Data were normalized using GCRMA. Genes with log2 expression values greater than 5 were considered to be expressed in brain tissue. The log fold-change (logFC) value was used as a measure of gene expression modulation and evaluated using Welch's t-test with Benjamini-Hochberg adjustment (P_{adj}). For affected genes with multiple probes, the data from the probe with the lowest P_{adj} was used. The precise methods for the comparison of logFC values between human ASDs and animal models were described in **Supplementary Methods**. Pathway analysis of marmoset genes was conducted using the IPA software (Qiagen, Summer Release 2020) and the precise methods were described also in **Supplementary Methods**.

Statistical analysis

All data are presented as mean ± s.e.m (n = dendrite or axon numbers) unless otherwise stated. The Mann-Whitney rank sum test was used to analyze the data shown in Figs. 1c, 1d, 2b, 3e, 4d, and 4f–h. The difference in probability distribution between cumulative plots was calculated using the Kolmogorov-Smirnov test, as shown in Figs. 1e, 1f, 2c, 2d and 4e. The differences between means were analyzed using the Friedman test, as shown in Figs. 5b, 5c, and the Kruskal-Wallis test in Figs. 6a–f. The Pearson's chi-square test was used to examine the frequency of the carryover spines and that of the total spines, with results shown in Figs. 3c and 3d. Fisher's exact test was also used to examine the spine survival rates for each condition in Fig. 1g, 3f. The *P*-values in Fig. 5j were obtained from the distribution of the simulation. The *r* and *P*-values in Figs. 7a and 7d show Pearson's correlation coefficients (r) and their *P*-values (P_r) against zero. The concordance values (c) and their *P*-values (P_c) in Fig. 7b show the number of genes exhibiting concordant changes between the animal model and human ASD divided by the total number of genes, and the probability was calculated using the one-sided binomial test. Other statistical tests are specified in the text or figure legends or elsewhere in the **Methods** section. Quantification, simulation, and statistical analysis were performed using Microsoft Excel, GraphPad Prism 9.3.1., and Real Statistics software (for Kolmogorov-Smirnov test; www.real-statistics.com.). Data collection and analysis were not performed in a blinded manner, and data were not randomized for analysis. No statistical methods were used to predetermine sample sizes, although our sample sizes are similar to those previously reported[17, 38].

Data availability

The microarray data generated in this study have been deposited at NCBI GEO under accession number GSE199560. All other data supporting the findings of this study are in **Supplementary Data 1-2**. All public domain data used in this study are listed in the **Methods** section and **Supplemental Methods** file.

642

643 ## References

644 1. Geschwind, D.H. & Levitt, P. Autism spectrum disorders: developmental
645 disconnection syndromes. *Curr Opin Neurobiol* **17**, 103-111 (2007).

646 2. Bourgeron, T. From the genetic architecture to synaptic plasticity in autism
647 spectrum disorder. *Nat Rev Neurosci* **16**, 551-563 (2015).

648 3. Webb, S.J., Neuhaus, E. & Faja, S. Face perception and learning in autism
649 spectrum disorders. *Q J Exp Psychol (Hove)* **70**, 970-986 (2017).

650 4. Esbensen, A.J., Seltzer, M.M., Lam, K.S. & Bodfish, J.W. Age-related
651 differences in restricted repetitive behaviors in autism spectrum disorders. *J*
652 *Autism Dev Disord* **39**, 57-66 (2009).

653 5. Djerassi, M., Ophir, S. & Atzil, S. What Is Social about Autism? The Role of
654 Allostasis-Driven Learning. *Brain Sci* **11** (2021).

655 6. Xu, T. *et al.* Rapid formation and selective stabilization of synapses for enduring
656 motor memories. *Nature* **462**, 915-919 (2009).

657 7. Hedrick, N.G. *et al.* Learning binds new inputs into functional synaptic clusters
658 via spinogenesis. *Nat Neurosci* **25**, 726-737 (2022).

659 8. Chen, J.L. & Nedivi, E. Neuronal structural remodeling: is it all about access?
660 *Curr Opin Neurobiol* **20**, 557-562 (2010).

661 9. Penzes, P., Cahill, M.E., Jones, K.A., VanLeeuwen, J.E. & Woolfrey, K.M.
662 Dendritic spine pathology in neuropsychiatric disorders. *Nat Neurosci* **14**, 285-
663 293 (2011).

664 10. Phillips, M. & Pozzo-Miller, L. Dendritic spine dysgenesis in autism related
665 disorders. *Neurosci Lett* **601**, 30-40 (2015).

666 11. Watanabe, S. *et al.* Functional and molecular characterization of a non-human
667 primate model of autism spectrum disorder shows similarity with the human
668 disease. *Nat Commun* **12**, 5388 (2021).

669 12. Antoine, M.W., Langberg, T., Schnepel, P. & Feldman, D.E. Increased
670 Excitation-Inhibition Ratio Stabilizes Synapse and Circuit Excitability in Four
671 Autism Mouse Models. *Neuron* **101**, 648-661 e644 (2019).

672 13. Fenelon, K. *et al.* The pattern of cortical dysfunction in a mouse model of a
673 schizophrenia-related microdeletion. *J Neurosci* **33**, 14825-14839 (2013).

674 14. Ash, R.T., Park, J., Suter, B., Zoghbi, H.Y. & Smirnakis, S.M. Excessive
675 Formation and Stabilization of Dendritic Spine Clusters in the MECP2-
676 Duplication Syndrome Mouse Model of Autism. *eNeuro* **8** (2021).

677 15. Isshiki, M. *et al.* Enhanced synapse remodelling as a common phenotype in
678 mouse models of autism. *Nat Commun* **5**, 4742 (2014).

679 16. Pan, F., Aldridge, G.M., Greenough, W.T. & Gan, W.B. Dendritic spine
680 instability and insensitivity to modulation by sensory experience in a mouse
681 model of fragile X syndrome. *Proc Natl Acad Sci U S A* **107**, 17768-17773
682 (2010).

683 17. Nagaoka, A. *et al.* Abnormal intrinsic dynamics of dendritic spines in a fragile X
684 syndrome mouse model in vivo. *Sci Rep* **6**, 26651 (2016).

685 18. Marlin, B.J. & Froemke, R.C. Oxytocin modulation of neural circuits for social
686 behavior. *Dev Neurobiol* **77**, 169-189 (2017).

687 19. Penagarikano, O. *et al.* Exogenous and evoked oxytocin restores social behavior
688 in the Cntnap2 mouse model of autism. *Sci Transl Med* **7**, 271ra278 (2015).

689 20. Sgritta, M. *et al.* Mechanisms Underlying Microbial-Mediated Changes in
690 Social Behavior in Mouse Models of Autism Spectrum Disorder. *Neuron* **101**,
691 246-259 e246 (2019).

692 21. Hara, Y. *et al.* Oxytocin attenuates deficits in social interaction but not
693 recognition memory in a prenatal valproic acid-induced mouse model of autism.
694 *Horm Behav* **96**, 130-136 (2017).

695 22. Parker, K.J. *et al.* Intranasal oxytocin treatment for social deficits and
696 biomarkers of response in children with autism. *Proc Natl Acad Sci U S A* **114**,
697 8119-8124 (2017).

698 23. Sikich, L. *et al.* Intranasal Oxytocin in Children and Adolescents with Autism
699 Spectrum Disorder. *N Engl J Med* **385**, 1462-1473 (2021).

700 24. Martins, D., Paduraru, M. & Paloyelis, Y. Heterogeneity in response to repeated
701 intranasal oxytocin in schizophrenia and autism spectrum disorders: A meta-
702 analysis of variance. *Br J Pharmacol* **179**, 1525-1543 (2022).

703 25. Yamasue, H. *et al.* Effect of a novel nasal oxytocin spray with enhanced
704 bioavailability on autism: a randomized trial. *Brain* (2022).

705 26. Boroviak, T. *et al.* Single cell transcriptome analysis of human, marmoset and
706 mouse embryos reveals common and divergent features of preimplantation
707 development. *Development* **145** (2018).

708 27. Koopmans, F. *et al.* Comparative Hippocampal Synaptic Proteomes of Rodents
709 and Primates: Differences in Neuroplasticity-Related Proteins. *Front Mol*
710 *Neurosci* **11**, 364 (2018).

711 28. Yasue, M. *et al.* Indifference of marmosets with prenatal valproate exposure to
712 third-party non-reciprocal interactions with otherwise avoided non-reciprocal
713 individuals. *Behav Brain Res* **292**, 323-326 (2015).

714 29. Yasue, M., Nakagami, A., Nakagaki, K., Ichinohe, N. & Kawai, N. Inequity
715 aversion is observed in common marmosets but not in marmoset models of
716 autism induced by prenatal exposure to valproic acid. *Behav Brain Res* **343**, 36-
717 40 (2018).

718 30. Nakagami, A. *et al.* Reduced childhood social attention in autism model
719 marmosets predicts impaired social skills and inflexible behavior in adulthood.
720 *Frontiers in Psychiatry* **13** (2022).

721 31. Parikshak, N.N. *et al.* Integrative functional genomic analyses implicate specific
722 molecular pathways and circuits in autism. *Cell* **155**, 1008-1021 (2013).

723 32. Freeman, S.M. & Young, L.J. Comparative Perspectives on Oxytocin and
724 Vasopressin Receptor Research in Rodents and Primates: Translational
725 Implications. *J Neuroendocrinol* **28** (2016).

33. Watanabe, T. *et al.* Diminished medial prefrontal activity behind autistic social judgments of incongruent information. *PLoS One* **7**, e39561 (2012).

34. Frank, A.C. *et al.* Hotspots of dendritic spine turnover facilitate clustered spine addition and learning and memory. *Nat Commun* **9**, 422 (2018).

35. Fu, M., Yu, X., Lu, J. & Zuo, Y. Repetitive motor learning induces coordinated formation of clustered dendritic spines in vivo. *Nature* **483**, 92-95 (2012).

36. Moda-Sava, R.N. *et al.* Sustained rescue of prefrontal circuit dysfunction by antidepressant-induced spine formation. *Science* **364** (2019).

37. Mullins, C., Fishell, G. & Tsien, R.W. Unifying Views of Autism Spectrum Disorders: A Consideration of Autoregulatory Feedback Loops. *Neuron* **89**, 1131-1156 (2016).

38. Sadakane, O. *et al.* In Vivo Two-Photon Imaging of Dendritic Spines in Marmoset Neocortex. *eNeuro* **2** (2015).

39. Santisakultarm, T.P. *et al.* Two-photon imaging of cerebral hemodynamics and neural activity in awake and anesthetized marmosets. *J Neurosci Methods* **271**, 55-64 (2016).

40. Holtmaat, A., Wilbrecht, L., Knott, G.W., Welker, E. & Svoboda, K. Experience-dependent and cell-type-specific spine growth in the neocortex. *Nature* **441**, 979-983 (2006).

41. Yasumatsu, N., Matsuzaki, M., Miyazaki, T., Noguchi, J. & Kasai, H. Principles of long-term dynamics of dendritic spines. *J Neurosci* **28**, 13592-13608 (2008).

42. Noguchi, J. *et al.* Bidirectional in vivo structural dendritic spine plasticity revealed by two-photon glutamate uncaging in the mouse neocortex. *Sci Rep* **9**, 13922 (2019).

43. Harvey, C.D., Yasuda, R., Zhong, H. & Svoboda, K. The spread of Ras activity triggered by activation of a single dendritic spine. *Science* **321**, 136-140 (2008).

44. Harvey, C.D. & Svoboda, K. Locally dynamic synaptic learning rules in pyramidal neuron dendrites. *Nature* **450**, 1195-1200 (2007).

754 45. Murakoshi, H., Wang, H. & Yasuda, R. Local, persistent activation of Rho
755 GTPases during plasticity of single dendritic spines. *Nature* **472**, 100-104
756 (2011).

757 46. Takahashi, N. *et al.* Locally synchronized synaptic inputs. *Science* **335**, 353-356
758 (2012).

759 47. Santamaria, F., Wils, S., De Schutter, E. & Augustine, G.J. The diffusional
760 properties of dendrites depend on the density of dendritic spines. *Eur J Neurosci*
761 **34**, 561-568 (2011).

762 48. Belmonte, M.K. *et al.* Autism and abnormal development of brain connectivity.
763 *J Neurosci* **24**, 9228-9231 (2004).

764 49. Ouyang, M., Kang, H., Detre, J.A., Roberts, T.P.L. & Huang, H. Short-range
765 connections in the developmental connectome during typical and atypical brain
766 maturation. *Neurosci Biobehav Rev* **83**, 109-122 (2017).

767 50. Holderith, N. *et al.* Release probability of hippocampal glutamatergic terminals
768 scales with the size of the active zone. *Nat Neurosci* **15**, 988-997 (2012).

769 51. Meltzer, A. & Van de Water, J. The Role of the Immune System in Autism
770 Spectrum Disorder. *Neuropsychopharmacology* **42**, 284-298 (2017).

771 52. Aoki, Y. *et al.* Absence of age-related prefrontal NAA change in adults with
772 autism spectrum disorders. *Transl Psychiatry* **2**, e178 (2012).

773 53. Kastellakis, G., Cai, D.J., Mednick, S.C., Silva, A.J. & Poirazi, P. Synaptic
774 clustering within dendrites: an emerging theory of memory formation. *Prog*
775 *Neurobiol* **126**, 19-35 (2015).

776 54. Reiner, B.C. & Dunaevsky, A. Deficit in motor training-induced clustering, but
777 not stabilization, of new dendritic spines in FMR1 knock-out mice. *PLoS One*
778 **10**, e0126572 (2015).

779 55. Bloss, E.B. *et al.* Single excitatory axons form clustered synapses onto CA1
780 pyramidal cell dendrites. *Nat Neurosci* **21**, 353-363 (2018).

781 56. Wilson, D.E., Whitney, D.E., Scholl, B. & Fitzpatrick, D. Orientation selectivity
782 and the functional clustering of synaptic inputs in primary visual cortex. *Nat*
783 *Neurosci* **19**, 1003-1009 (2016).

784 57. Hiratani, N. & Fukai, T. Redundancy in synaptic connections enables neurons to
785 learn optimally. *Proc Natl Acad Sci U S A* **115**, E6871-E6879 (2018).

786 58. Yamasue, H. *et al.* Effect of intranasal oxytocin on the core social symptoms of
787 autism spectrum disorder: a randomized clinical trial. *Mol Psychiatry* **25**, 1849-
788 1858 (2020).

789 59. Benner, S. *et al.* Neurochemical evidence for differential effects of acute and
790 repeated oxytocin administration. *Mol Psychiatry* **26**, 710-720 (2021).

791 60. Schorscher-Petcu, A., Dupre, A. & Tribollet, E. Distribution of vasopressin and
792 oxytocin binding sites in the brain and upper spinal cord of the common
793 marmoset. *Neurosci Lett* **461**, 217-222 (2009).

794 61. Sahin, M. & Sur, M. Genes, circuits, and precision therapies for autism and
795 related neurodevelopmental disorders. *Science* **350** (2015).

796 62. Ash, R.T. *et al.* Inhibition of Elevated Ras-MAPK Signaling Normalizes
797 Enhanced Motor Learning and Excessive Clustered Dendritic Spine
798 Stabilization in the MECP2-Duplication Syndrome Mouse Model of Autism.
799 *eNeuro* **8** (2021).

800 63. Noguchi, J. *et al.* State-dependent diffusion of actin-depolymerizing
801 factor/cofilin underlies the enlargement and shrinkage of dendritic spines. *Sci*
802 *Rep* **6**, 32897 (2016).

803 64. Liston, C. & Gan, W.B. Glucocorticoids are critical regulators of dendritic spine
804 development and plasticity in vivo. *Proc Natl Acad Sci U S A* **108**, 16074-16079
805 (2011).

806 65. Frye, C.A. & Llaneza, D.C. Corticosteroid and neurosteroid dysregulation in an
807 animal model of autism, BTBR mice. *Physiol Behav* **100**, 264-267 (2010).

66. Lorsung, E., Karthikeyan, R. & Cao, R. Biological Timing and Neurodevelopmental Disorders: A Role for Circadian Dysfunction in Autism Spectrum Disorders. *Front Neurosci* **15**, 642745 (2021).

67. Nakamura, M. *et al.* Prenatal valproic acid-induced autism marmoset model exhibits higher salivary cortisol levels. *Frontiers in Behavioral Neuroscience* **16** (2022).

68. Schindelin, J. *et al.* Fiji: an open-source platform for biological-image analysis. *Nat Methods* **9**, 676-682 (2012).

69. Grillo, F.W. *et al.* Increased axonal bouton dynamics in the aging mouse cortex. *Proc Natl Acad Sci U S A* **110**, E1514-1523 (2013).

70. Cavanaugh, J., Huffman, M.C., Harnisch, A.M. & French, J.A. Marmosets treated with oxytocin are more socially attractive to their long-term mate. *Front Behav Neurosci* **9**, 251 (2015).

Acknowledgments

We thank H. Kasai of The University of Tokyo for helpful discussion and suggestions about two-photon imaging, and H. Yamasue of Hamamatsu University School of Medicine and T. Minamimoto of QST, Japan, for careful reading of the manuscript. We are also grateful to T. Araki and M. Iwasaki of the National Center of Neurology and Psychiatry (NCNP) for helpful discussion about experiments and marmoset surgery, respectively. We also thank A. Tsuchiya, W. Suzuki, A. Mishima, K. Mimura, and N. Miyakawa of our lab for supporting primate experiments, and R. Saito, Y. Katakai, and other members of the NCNP primate facility for caring for VPA-exposed and UE marmosets. A. Sawatari and S. Ikeda of Iwate University assisted with spine volume analysis. This work was supported by Intramural Research Grants for Neurological and Psychiatric Disorders from the NCNP (3-5, J.N. and 29-6, N.I.), a Novartis Research Grant 2019 (S.W.), JSPS KAKENHI Grant Numbers JP18K06497 and JP22K07363 (J.N.), and AMED Grant Number JP21dm0207066 (N.I.).

Author contributions

J.N. and N.I. designed the study; J.N., S.W., R.I., and K.S. performed the in vivo two-photon imaging; K.N. created the autism model marmosets; J.N. and R.I. conducted image analyses; E. S., H.T., H.M., A.W., and T.Y. prepared the AAV vectors.; S.W., T.O., K.S., K.H., K.S., and I.M. conducted the microarray analysis.; J.N. and N.I. wrote the manuscript. All authors agreed to the manuscript of the paper.

Competing interests

The authors declare that they have no conflicts of interest.

Additional information

Supplementary information **Supplementary Methods** (attached at the end of this manuscript), **Supplementary Data 1** and **2** (omitted)

Correspondence and requests for data should be addressed to J.N. or N.I.

Supplementary Methods

Comparison of log fold change (logFC) values between human autism spectrum disorder (ASD) and animal models, as determined by the coexpression modules.

To examine gene expression changes in the ASD group compared to the typically developed human group or in the ASD model animals compared to the controls, logFC values were calculated for the genes analyzed by the gene chip. The concordance values were then calculated for each gene module[1, 2] to show consistency in the direction of gene expression changes between human ASD and the animal models (Fig. 7c). Practically, the concordance value was the percentage of genes that changed in a common direction (first and third quadrants in Fig. 7a, b, d) in human ASD and the model animal. For modules with at least 8 common genes between the animal model and human ASD, the concordance values were shown by the color in Fig. 7c. The logFC values of VPA rats[3] (35–day), BTBR mice[4] (4–month), FMR1 mice[5] (8-14–week), MeCP2 heterozygous mice[6] (5–week), Tcf4 mice[7] (60-80–day), 15q13 mice[8] (10-22–week), and Pten^{m3m4} mice[9] (6–week) were obtained from the literatures previously published; The numbers in parentheses show their age. To compare gene expression modulations in the marmoset model with those in human ASD of postmortem samples[2], commonly modulated genes with $P_{adj} < 0.1$ were used. For the rat VPA models and BTBR mice, the genes with $P_{adj} < 0.05$ were selected; for other models and human ASD, $P_{adj} < 0.1$ were selected. To compare gene expression modulations in the rodent models with those in human ASD, gene symbols were converted using HomoloGene (NCBI, https:// www.ncbi.nlm.nih.gov/homologene, release 68). Due to the small number of genes that are commonly affected, mouse models of maternal immune activation[10] and Shank3 knockout[11] were not included in the list.

Signaling pathway estimation of marmoset genes

878 Pathway analysis of marmoset genes was conducted using the IPA software (Qiagen, Summer
879 Release 2020). Brain cell type (neuron, astrocyte, microglia, oligodendrocyte, and endothelial
880 cell) specific genes were selected from genes with mean logFC gene enrichment values > 2, in
881 the top ranked cell type-enriched genes based on the human single cell analysis data in the
882 previous report[12].
883

884 **References**

885 1. Parikshak, N.N. *et al.* Integrative functional genomic analyses implicate specific
886 molecular pathways and circuits in autism. *Cell* **155**, 1008-1021 (2013).
887 2. Parikshak, N.N. *et al.* Genome-wide changes in lncRNA, splicing, and regional
888 gene expression patterns in autism. *Nature* **540**, 423-427 (2016).
889 3. Zhang, R. *et al.* Transcriptional and splicing dysregulation in the prefrontal cortex
890 in valproic acid rat model of autism. *Reprod Toxicol* **77**, 53-61 (2018).
891 4. Mizuno, S. *et al.* Comprehensive Profiling of Gene Expression in the Cerebral
892 Cortex and Striatum of BTBRTF/ArtRbrc Mice Compared to C57BL/6J Mice.
893 *Front Cell Neurosci* **14**, 595607 (2020).
894 5. Rogers, T.D. *et al.* Effects of a social stimulus on gene expression in a mouse
895 model of fragile X syndrome. *Mol Autism* **8**, 30 (2017).
896 6. Zhao, D. *et al.* Transcriptome analysis of microglia in a mouse model of Rett
897 syndrome: differential expression of genes associated with microglia/macrophage
898 activation and cellular stress. *Mol Autism* **8**, 17 (2017).
899 7. Phan, B.N. *et al.* A myelin-related transcriptomic profile is shared by Pitt-Hopkins
900 syndrome models and human autism spectrum disorder. *Nat Neurosci* **23**, 375-
901 385 (2020).

902 8. Gordon, A. *et al.* Transcriptomic networks implicate neuronal energetic
903 abnormalities in three mouse models harboring autism and schizophrenia-
904 associated mutations. *Mol Psychiatry* **26**, 1520-1534 (2021).
905 9. Tilot, A.K. *et al.* Neural transcriptome of constitutional Pten dysfunction in mice
906 and its relevance to human idiopathic autism spectrum disorder. *Mol Psychiatry*
907 **21**, 118-125 (2016).
908 10. Smith, S.E., Li, J., Garbett, K., Mirnics, K. & Patterson, P.H. Maternal immune
909 activation alters fetal brain development through interleukin-6. *J Neurosci* **27**,
910 10695-10702 (2007).
911 11. Qin, L. *et al.* Social deficits in Shank3-deficient mouse models of autism are
912 rescued by histone deacetylase (HDAC) inhibition. *Nat Neurosci* **21**, 564-575
913 (2018).
914 12. McKenzie, A.T. *et al.* Brain Cell Type Specific Gene Expression and Co-
915 expression Network Architectures. *Sci Rep* **8**, 8868 (2018).
916